AD NUMBER

AD-356 903

CLASSIFICATION CHANGES

TO **UNCLASSIFIED**

FROM **CONFIDENTIAL**

AUTHORITY

OCA; Dec 31, 1976

19990226100

AD NUMBER

AD-356 903

NEW LIMITATION CHANGE

TO **DISTRIBUTION STATEMENT - A**

Approved for public release;
distribution is unlimited.

LIMITATION CODE: 1

FROM **B/3**

AUTHORITY

AFATL via Ltr; Nov 1, 1977

ATL-TR-64-83

(U) HYPERVELOCITY IMPACT EXPERIMENTS

Technical Report No. ATL-TR-64-83
December 1964 Project No. 9650

Directorate of Armament Development
Det 4, Research and Technology Division
Air Force Systems Command
Eglin Air Force Base, Florida

(Prepared under Contract AF 08(635)-2793 by General Motors Corporation, GM Defense Research Laboratories, Santa Barbara, California)

ABSTRACT

This final report describes the experimental results of a program conducted under Contract AF08(635)-2783, "Hypervelocity Impact Experiments," to investigate the vulnerability of multiple sheet thin target assemblies to hypervelocity projectiles impacting at both normal and oblique angles. This study of penetration, perforation and spalling was conducted using an accelerated-reservoir light-gas gun to launch projectiles to velocities ranging from 5000 fps to 25,500 fps. Projectile incident angles ranged from 90 degrees (normal) to 10 degrees.

Target damage was evaluated in terms of hole area, depth of penetration and affected area. Damage was correlated with impact velocity, impact angle, projectile variables, and target variables.

This report has been reviewed and is approved.

DAVID K. DEAN
Colonel, USAF
Chief, Weapons Division

CONTENTS

ILLUSTRATIONS

ILLUSTRATIONS (continued)

LIST OF SYMBOLS

A_1	Shield perforation or hole area
A_o	Normal projectile area, $A_o = \frac{\pi d^2}{4}$
α	Shield angle of incidence – smallest angle measured from the shield to the projectile flight line
α_1	Shield angle below which projectile ricochet occurs and above which perforation occurs
α^*	Shield angle below which there is no subsequent damage from in-line spray particles, i.e., no target damage in the direction of the projectile flight line
β	Target sheet angle of incidence – smallest angle measured from the target to the projectile flight line
BHN	Brinell Hardness Number
γ	Projectile-spray semi-angle
θ	Spall-spray semi-angle
d	Normal projectile diameter
D	Perforation diameter in normal shield
D_{major}	Maximum length of the shield perforation
D_{minor}	Maximum width of the shield perforation
ρ_P	Projectile material density
ρ_T	Target (shield) material density
t_s	Normal sheet thickness
P	Penetration

SECTION I
INTRODUCTION

Of current interest to the Air Force in their Space Program is the investigation of non-nuclear kill mechanisms from both offensive and defensive viewpoints. Offensively, this interest has led to enhanced lethality concepts for warhead development. Defensively, it has led to advances in the science of spacecraft design. One of the problems is the vulnerability of spacecraft to impacts of hypervelocity fragments, since such a collision could result in the defeat of a mission. It is necessary, therefore, to devise means of protecting a spacecraft from these fragments while remaining aware of the penalties involved in increasing the vehicle gross weight or unduly complicating its structure.

Although many configurations of vehicle hulls have been proposed, the foremost, and one of the original concepts, is that of a thin outer shell separated from and protecting the main hull.[1] In theory, any meteoroid or warhead fragment that impacted this outer shell would vaporize before it could penetrate the main hull – in practice, however, this appears generally possible only at very high velocities, for the actual physical mechanism of impact that has been observed at typical encounter velocities does not include vaporization of fragments.[2]

Figure 1 is an artist's representation of the impact of a solid sphere against such a thin target, the protective outer shell. The projectile strikes the target and, because of the intense pressures developed, generates a shock wave in both projectile and target. These shocks cause the projectile to break up into a multitude of tiny fragments, producing an expanding bubble of debris with a velocity component normal to the shield that is generally less than the velocity of the original projectile. The result of these factors of fragment spread and velocity reduction is that the protected hull is subjected to less momentum and energy loading per unit area than an unprotected hull.

While it is true that this design concept should reduce the vehicle vulnerability, the mode and magnitude of impact damage still required study. Since the number of possible target configurations is virtually unlimited, a typical multisheet thin target assembly was chosen to be subjected to impacts of specific projectiles under specific encounter conditions.

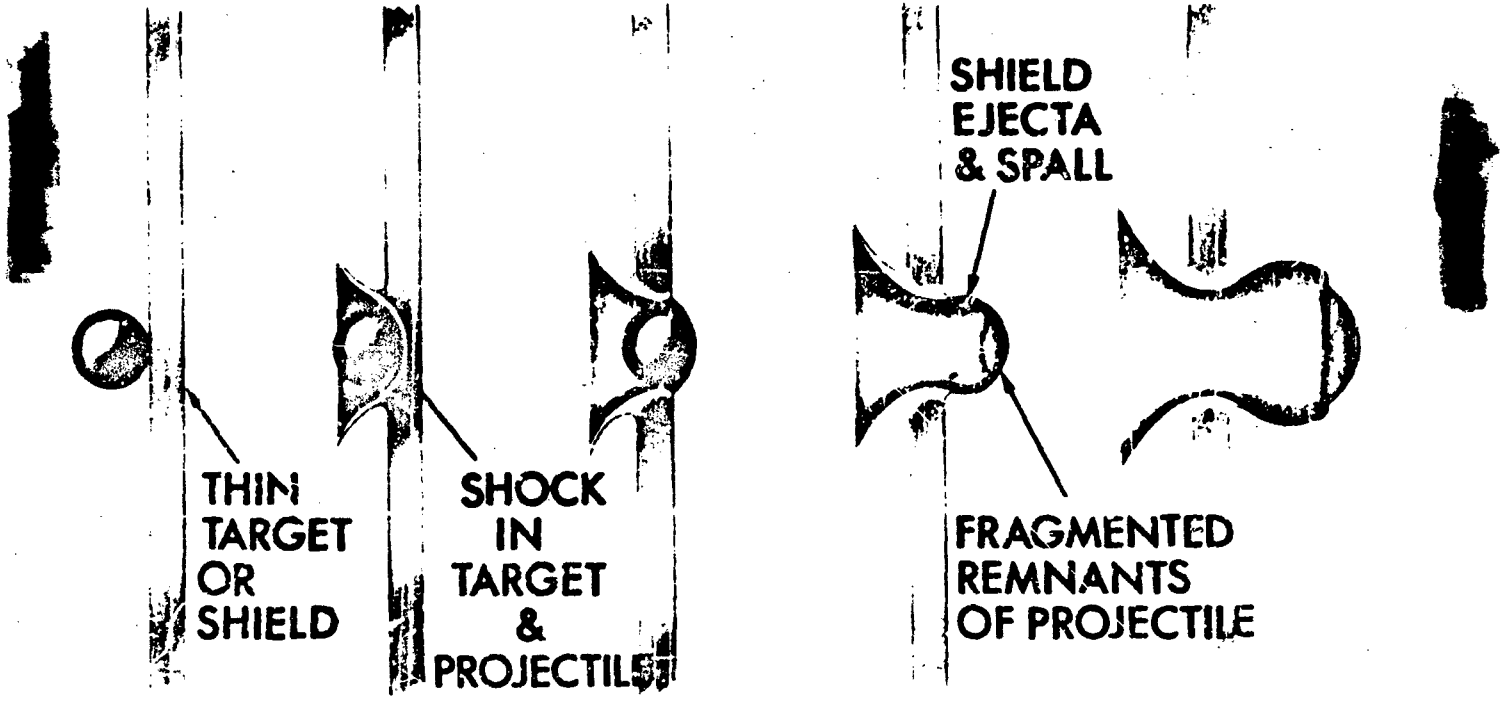

Fig. 1 Projectile and Shield Behavior Upon Impact of a Solid Sphere with Thin Target

[redacted]

The basic thin target assembly consisted of two 2014-T6 aluminum sheets spaced twelve inches apart. The experimental variables were those of the projectile (material, mass, velocity, angle of impact) and those of the target assembly (material, intersheet spacing, angle of impact).

Other tests, conducted concurrently, were to investigate the phenomenon of impact flash and its potential use as a hit director and target discriminator.

[redacted]

(This page is intentionally blank)

SECTION II

TECHNICAL ACTIVITIES AND RESULTS

2.1 Experimental Facility

The experiments in this program were conducted at GM Defense Research Laboratories (Ref. 3) on Ballistics Ranges 'C' and 'D'. The launchers were respectively, a .22-caliber smooth bore powder gun or a 20-mm accelerated-reservoir light-gas gun (ARLGG), and a .30-caliber ARLGG. The powder gun was used when velocities below 10,000 fps were required, and the ARLGG, guns were used for velocities above 10,000 fps. The .30-caliber ARLGG, however, was capable of launching only low weight projectiles ($m < 0.3$ gm) at velocities in excess of 25,000 fps; consequently, most of the tests were made with the 20-mm ARLGG. This gun and the associated range complex are shown schematically in Fig. 2. Following is a brief description.

2.1.1 20-mm ARLG Gun

The accelerated-reservoir light-gas gun was selected because it maintains a constant pressure at the base of the model during the launching cycle. This constant base pressure produces a constant, yet moderate, acceleration of the model throughout its travel down the barrel. Hence, the model achieves a high muzzle velocity without being loaded to the point of deformation or failure. This type of gun, then, is the logical choice for launching fragile models or saboted projectiles of high mass and high density.

2.1.2 Surge-Tank/Flight-Range/Velocity-Chamber Complex

This complex provides, in order:

(1) Tanks that confine the muzzle blast and allow the high-pressure, high-temperature driver gas to expand and cool

(2) Tanks that contain a controlled atmosphere in which the sabot separates from the model. The downrange end of the flight range is the sabot trap where the sabot petals are stopped, allowing the model to proceed alone.

(3) Tanks that house spark shadowgraph instrumentation (Fig. 3a) to establish projectile velocity, orientation, and integrity during each firing. Two successive spark shadowgraph pictures of the projectile, taken along its trajectory over a distance of eighteen inches (Fig. 3b), are combined with the elapsed times obtained from chronographs to determine velocities with an accuracy of ± 1 percent. The spark shadowgraphs also show the flight orientation of the projectile, record whether it has separated properly from its sabot, and establish its trajectory.

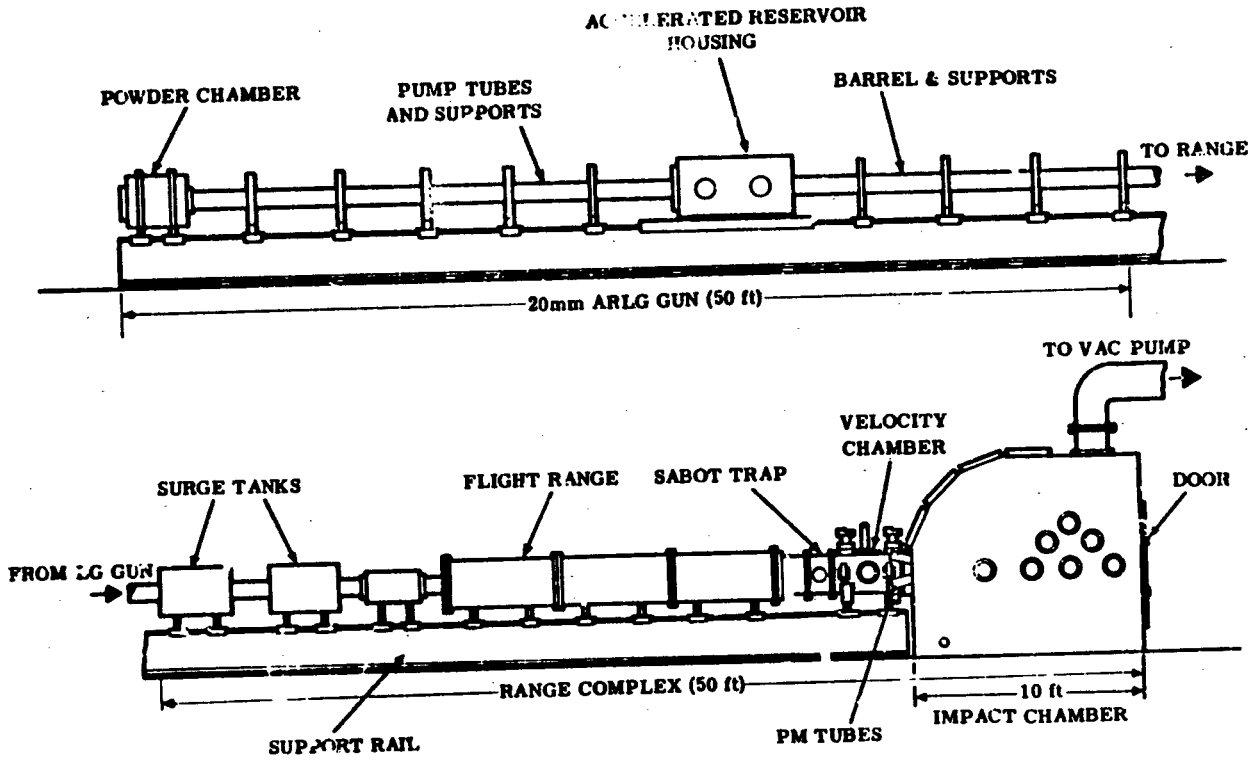

Fig. 2 Schematic of Ballistic Range 'C'

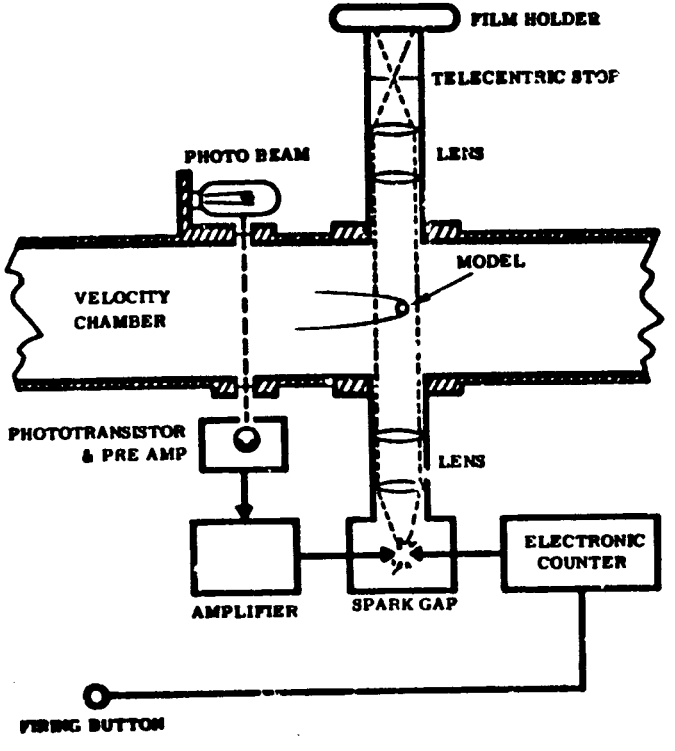

Fig. 3a Schematic of Spark Shadowgraph Velocity Station

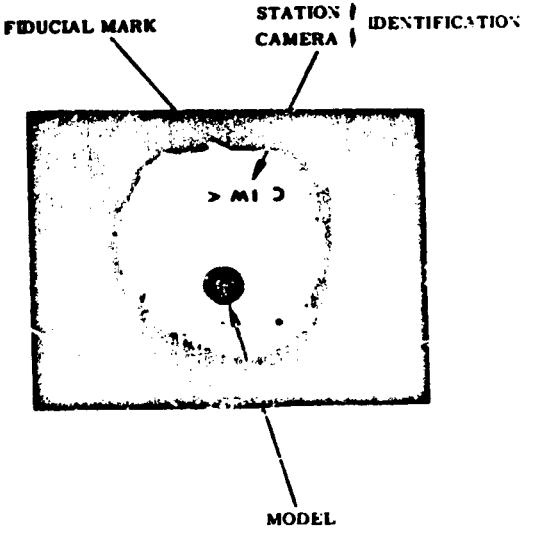

Fig. 3b Typical Spark Shadowgraph

[redacted]

2.1.3 Impact Chamber

This chamber was specially constructed to house the large target sheets needed to study spray distributions when the distance between shield and target is large. The impact chamber has numerous viewing ports to accommodate the instrumentation, and the rear wall of the chamber is a full-size door to allow easy installation and removal of the targets. The targets are held by a mount attached to the floor and walls. The surge-tank/flight-range/velocity-chamber/impact-chamber assembly is vacuum-sealed and can be evacuated to pressures of less than 10^{-3} torr, equivalent to a pressure-altitude of approximately 300,000 feet.

The impact of the projectile and the reaction of the target can be observed by both the 0.07-microsecond, two-channel flash radiography system and the 1.4-million-frames-per-second Beckman-Whitley framing camera. The choice of instrumentation depends upon the specific observations to be made of a given shot. The impact flash is monitored by both photomultiplier (PM) tubes and an indium-antimonide (InSb) infrared detector. The PM tubes are sensitive to the following wavelengths: (a) 1800A to 5500A, (b) 4500A to 10,000A, (c) 5940A to 10,000A. The InSb detector is sensitive to radiation in the region from 1 to 5 microns. These detectors are calibrated to measure radiation in watts per unit-solid-angle.

Preliminary firings were carried out prior to the data rounds to develop sabot designs and deflection techniques and to optimize the internal ballistics of the gun operating cycle. These firings also served as proof rounds for the impact chamber instrumentation.

2.2 Experimental Results

2.2.1 Experimental Program

The experimental program, as stated, consisted of firing specific hypervelocity projectiles into a typical multisheet target assembly under specific encounter conditions. This target assembly is shown schematically in Fig. 5 which also details the experimental variables.

A comprehensive synopsis of the raw impact data obtained during the investigation is attached to this report as Appendix I. Not included in the appendix is reduced data from a complimentary study involving hypervelocity impacts at angles of incidence ranging from 2 to 15 degrees, although this additional information has been included to extend the scope of the discussion of the experimental results. The impact flash data is attached as Appendix II. Table 1 lists typical physical and mechanical properties of the projectile and target materials.

[redacted]

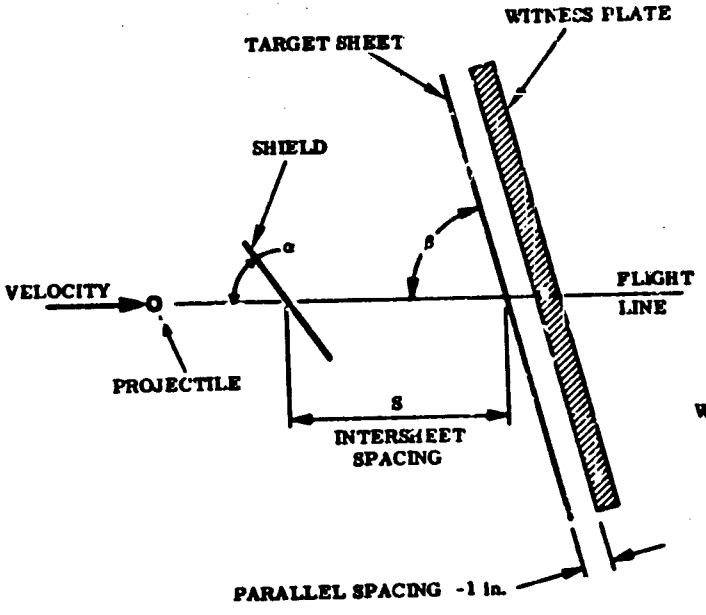

Fig. 4a Schematic of Typical Multisheet Thin Target Assembly

PROJECTILE MATERIAL: 2017 ALUMINUM, NICKEL "200"
MASS: 0.047 gm – 1.5 gm
SHAPE: $1/3 \leq l/d \leq 3$
VELOCITY: 8,000 fps – 25,500 fps

SHIELD MATERIAL: 2014-T6 ALUMINUM, TYPE 302 STAINLESS STEEL
$\alpha = 10^{\circ} \leq \alpha^{\circ} \leq 90^{\circ}$

INTERSHEET SPACING: 4, 6, 12, 24 (INCHES)

TARGET MATERIAL: 2014-T6 ALUMINUM, TYPE 302 STAINLESS STEEL
$\beta = 45^{\circ}, 60^{\circ}, 90^{\circ}$

WITNESS PLATE MATERIAL: 2014-T6 ALUMINUM

Fig. 4b Experimental Variables

Table 1

TYPICAL MATERIAL PROPERTIES
PHYSICAL AND MECHANICAL

	Projectile Materials			Target Materials		
	2017 Aluminum	Nickel "200"	Depleted Uranium	2014-T6 Aluminum	AISI Type 302 Stainless Steel	ASTM Type AZ31B-H24 Magnesium
Physical properties:						
Density – lb/cu in.	0.101	0.32	0.69	0.101	0.29	0.064
Melting Point – ^{o}F	1200	2635	2070	1200	2550 – 2590	1050 – 1170
Mechanical properties:						
Tensile yield strength kpsi	40	30	35 to 60	53	75	37
Ultimate strength kpsi	62	70	75 to 110	60	110	45
Hardness	R_B 35	70 BHN	R_B 65–90	135 BHN	R_B 85	R_B 20–30

2.3 Shield Analysis

Shield damage may be analyzed in many ways, and the resulting data may take many forms. (Ref. 4) For this program, however, only the gross damage has been considered; this is best represented by the perforation area or hole area, A_1. The holes discussed in this report are those through which a collimated light beam normal to the target plane can be projected onto photosensitive paper.

Typical of the results of this program are the perforations shown in Fig. 5 to demonstrate the effect of a changing angle of incidence, α (all other variables constant). It can be seen that the hole or perforation area, A_1, increases slowly from its normal value to a peak at an angle of approximately 35 degrees, and then decreases sharply as the angle of incidence is further decreased. It can also be seen that the hole becomes increasingly oval as α is decreased. These results are shown graphically in Fig. 6, where A_1 has been non-dimensionalized by dividing by the normal projectile area A_0, where

$$A_0 = \frac{\pi d^2}{4} \qquad (d = \text{projectile diameter})$$

The effect of hole shape has been plotted as D_{major}/D_{minor}, where D_{major} is the maximum length of the perforation and D_{minor} is the maximum width. Figure 7 shows the result of tests with the same combination of materials (Al – Al), but with a change in t_s/d to 0.4 (In Fig. 6, $t_s/d = 0.27$); t_s is the shield sheet thickness. It can be seen that the curve here is similar to that of Fig. 6, but it peaks at 45 degrees rather than 35 degrees. Substantial perforations were still evident at angles as low as 10 degrees, which was the final test angle of this series. Figures 8 and 9 demonstrate the effects of the impacts of nickel projectiles against stainless steel and aluminum shields, respectively. Although only three angular conditions have been tested in each case, it is felt that the curves are representative. Figure 8 is similar in shape to that of Halperson (Ref. 5); and Fig. 9 seemingly provides results similar to those of Fig. 10, which involves impacts of depleted uranium spheres against magnesium shields (from Ref. 6).

The experimental results of Al – Al impacts shown in Figs. 6 and 7 are combined in Fig. 11 to demonstrate the effect of shield thickness upon shield damage. Here it can be seen that, in the region $90 < \alpha^0 < 15$, the damage to the thicker sheet is more severe.

To consider the effect of projectile velocity on the extent of shield damage, it is necessary to refer again to the physical description of normal perforation introduced with Fig. 1. At extremely low velocities, the impact does not generate sufficient pressure to initiate the formation of shock waves, producing only elastic or shear waves. Consequently, the projectile

CONFIDENTIAL

PROJECTILE MATERIAL: 2017 ALUMINUM
DIAMETER: 0.375 IN.
VELOCITY: 25,000 fps

SHIELD MATERIAL: 2014-T6 ALUMINUM
THICKNESS: 0.100 IN.
t_s/d: 0.27

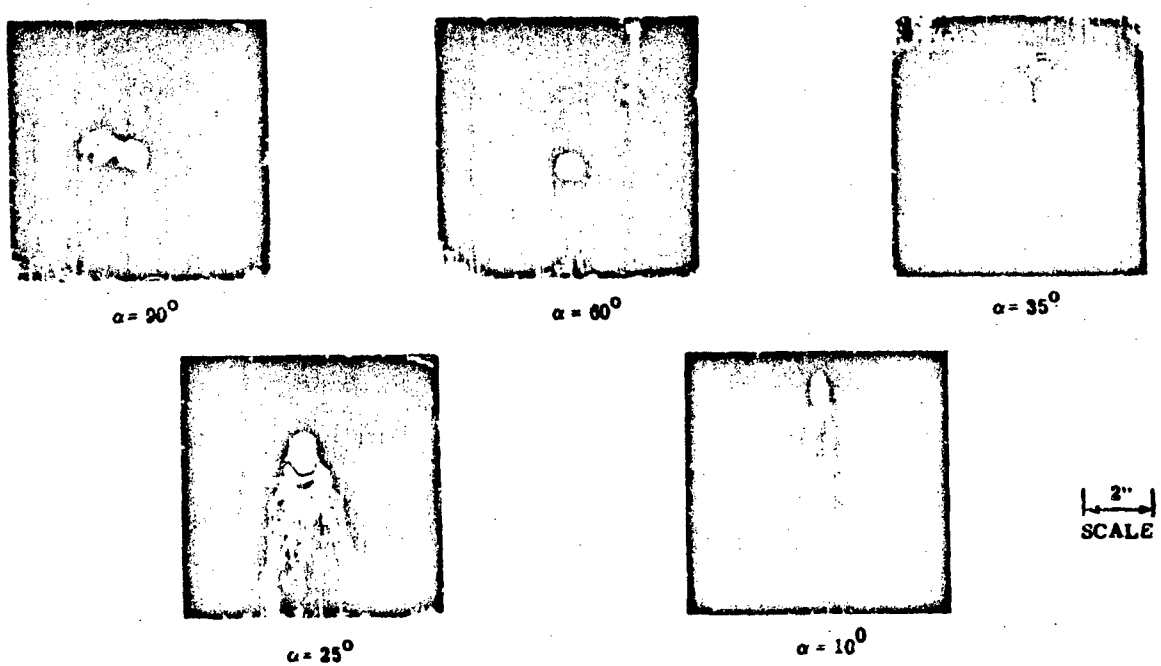

Fig. 5 Typical Shield Perforations – Effect of Varying Angle, Al → Al

PROJECTILE MATERIAL: 2017 ALUMINUM SHIELD MATERIAL: 2014-T6 ALUMINUM
DIAMETER: 0.375 IN.
VELOCITY: 25,000 fps t_s/d : 0.27

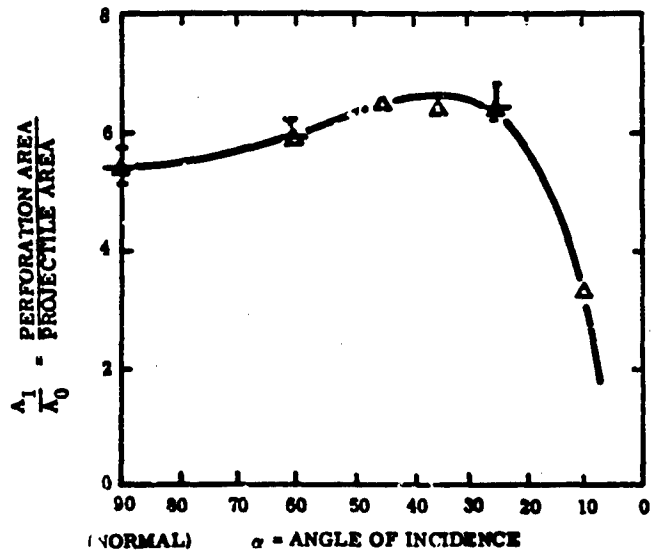

Fig. 6a Area of Perforation

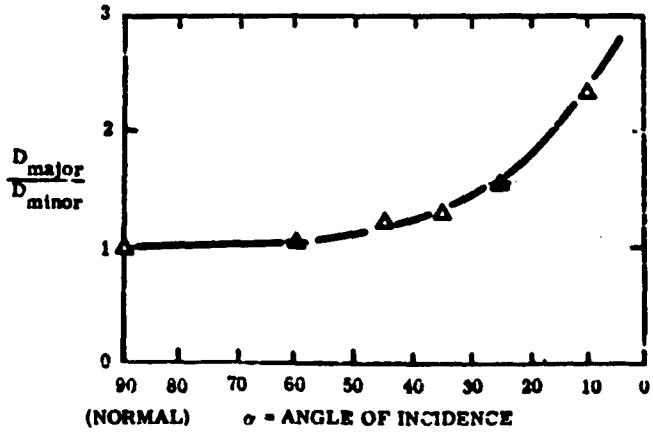

Fig. 6b Shape of Perforation

Fig. 6 Shield Damage, Al → Al (t_s/d = 0.27, v = 25,000 fps)

PROJECTILE MATERIAL: 2017 ALUMINUM SHIELD MATERIAL : 2014-T6 ALUMINUM
DIAMETER: 0.25 IN. t_s/d : 0.40
VELOCITY: 25,500 fps

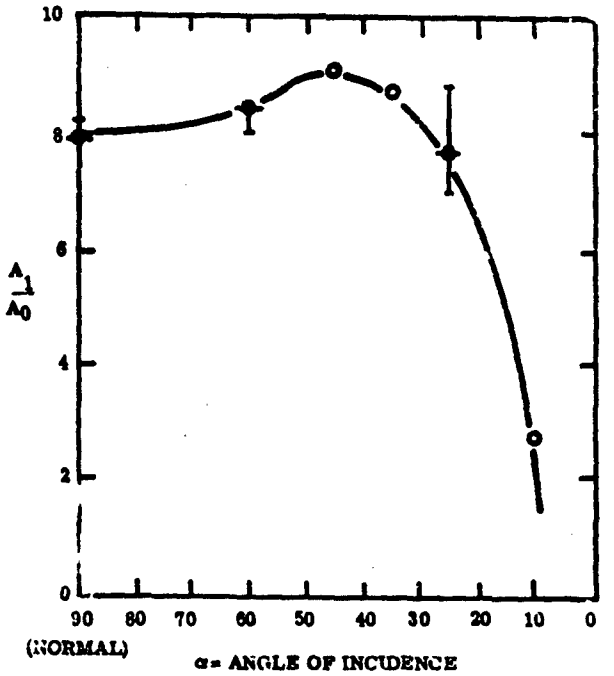

Fig. 7a Area of Perforation

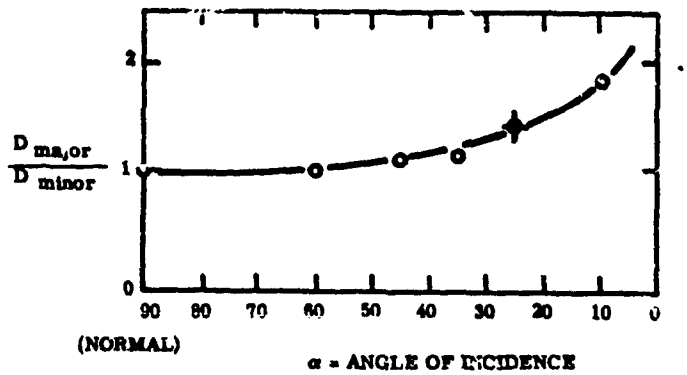

Fig. 7b Shape of Perforation

Fig. 7 Shield Damage, Al → Al (t_s/d = 0.40, v = 25,000 fps)

PROJECTILE MATERIAL: NICKEL "200"
DIAMETER: 0.107 IN.
VELOCITY: 25,000 fps

SHIELD MATERIAL: TYPE 302 STAINLESS STEEL
t_s/d : 0.150

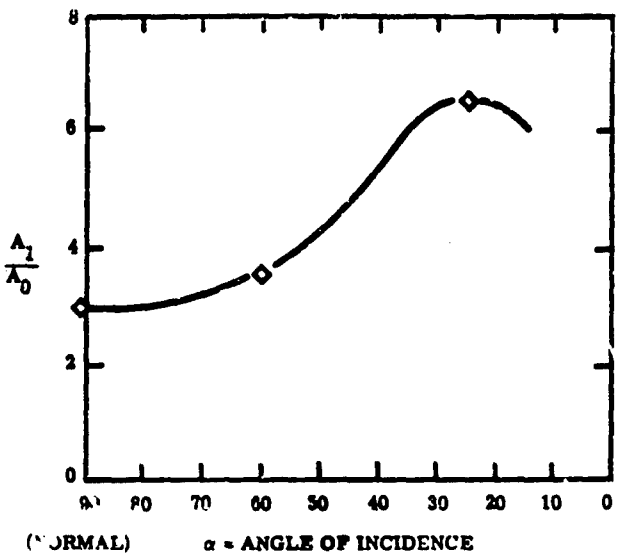

Fig. 8a Area of Perforation

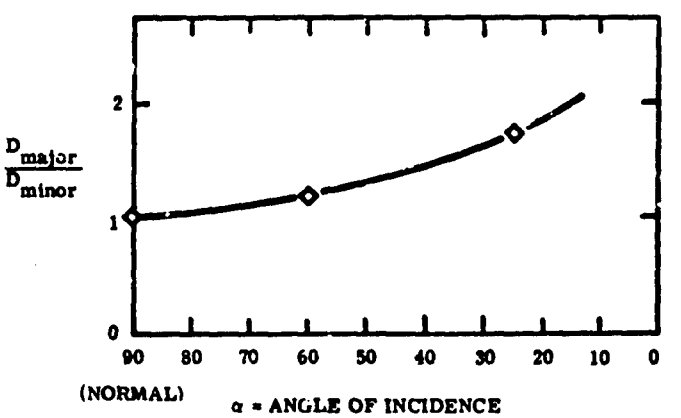

Fig. 8b Shape of Perforation

Fig. 8 Shield Damage, Ni → Stainless Steel (t_s/d = 0.15, v = 25,000 fps)

PROJECTILE MATERIAL: NICKEL "200" SHIELD MATERIAL: 2014-T6 ALUMINUM
DIAMETER. 0.187 IN. t_s/d = 0.534
VELOCITY: 25,000 fps

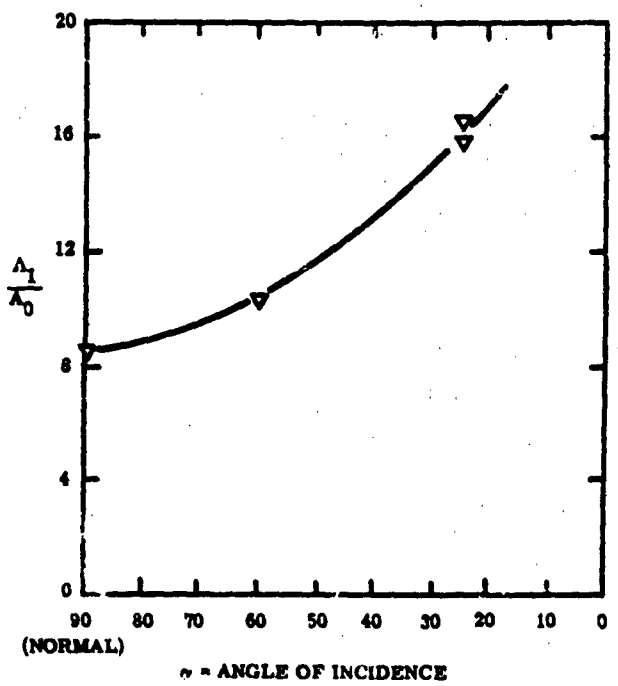

Fig. 9a Area of Perforation

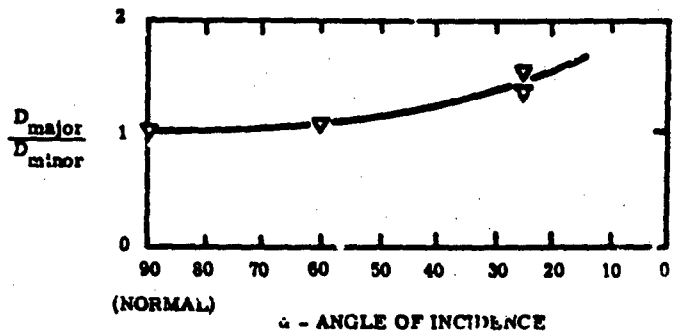

Fig. 9b Shape of Perforation

Fig. 9 Shield Damage, Ni → Al (t_s/d = 0.534, v = 25,000 fps)

PROJECTILE MATERIAL: DEPLETED URANIUM
DIAMETER: 0.143 IN.
VELOCITY: 23,350 fps

SHIELD MATERIAL: AZ31B-H24 MAGNESIUM
THICKNESS: 0.100 IN.
t_s/d : 0.70

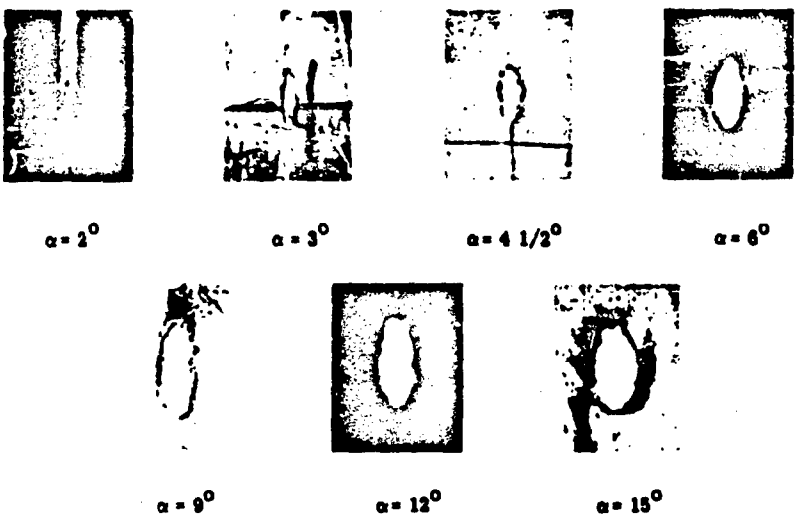

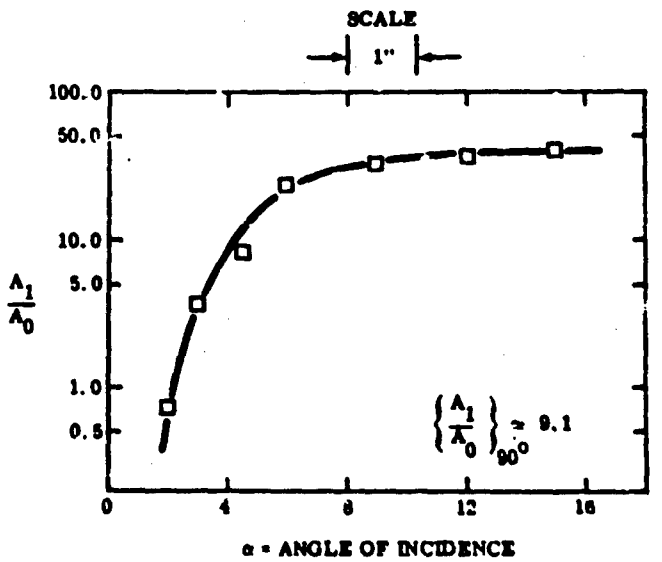

Fig. 10 Typical Shield Perforation – Effect of Varying Angle

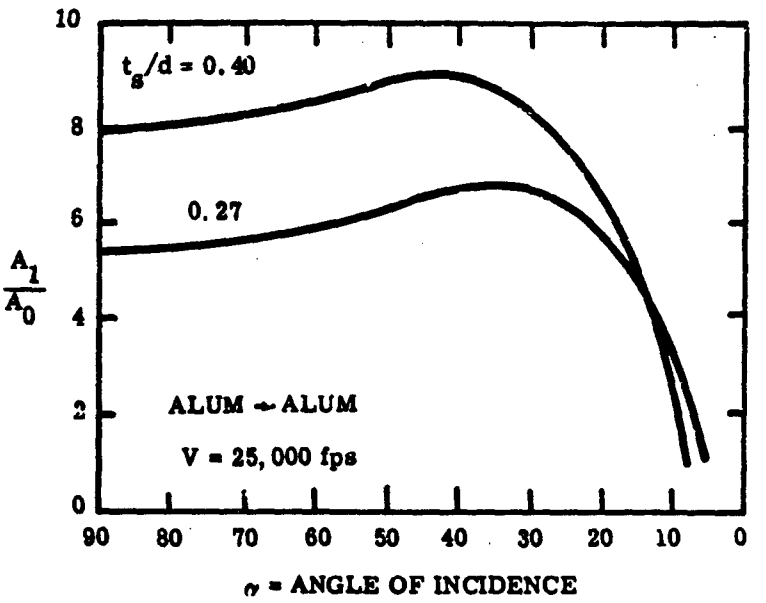

Fig. 11 Shield Damage, Effect of Variation of Sheet Thickness, Constant Velocity

suffers little damage during perforation. For a thick ductile shield, the edge of the hole is thickened due to the plastic flow. (Ref. 7) Brittle materials fail by punching; that is, a disc of approximately projectile size is sheared out of the shield. (Ref. 7) Thin sheets (small t_s/d) tend to fail by petalling. (Several simplified theories for these various modes of failure are reviewed in Reference 8.) At increased velocity, these elastic or shear waves are replaced by shock waves that result in hypervelocity impact phenomena. Perforations associated with hypervelocity for conditions of normal impact have been treated extensively, both theoretically and experimentally, in Refs. 9 and 10. These demonstrate that the process of fracture of projectile and shield can be interpreted as a multiple-spalling phenomenon which starts at the free surfaces, and that the hole area ratio increases linearly with velocity.

Al → Al normal impacts (Fig. 12) generated during the course of this program compare favorably with those predicted by Equation (1) from Ref. 10, i.e.,

$$\frac{A_1}{A_0} = \left\{\frac{D}{d}\right\}^2 = \left\{0.1372\, v \left(\frac{t_s}{d}\right)^{2/3} + 0.90\right\}^2 \qquad \text{(Ref. 10).}$$

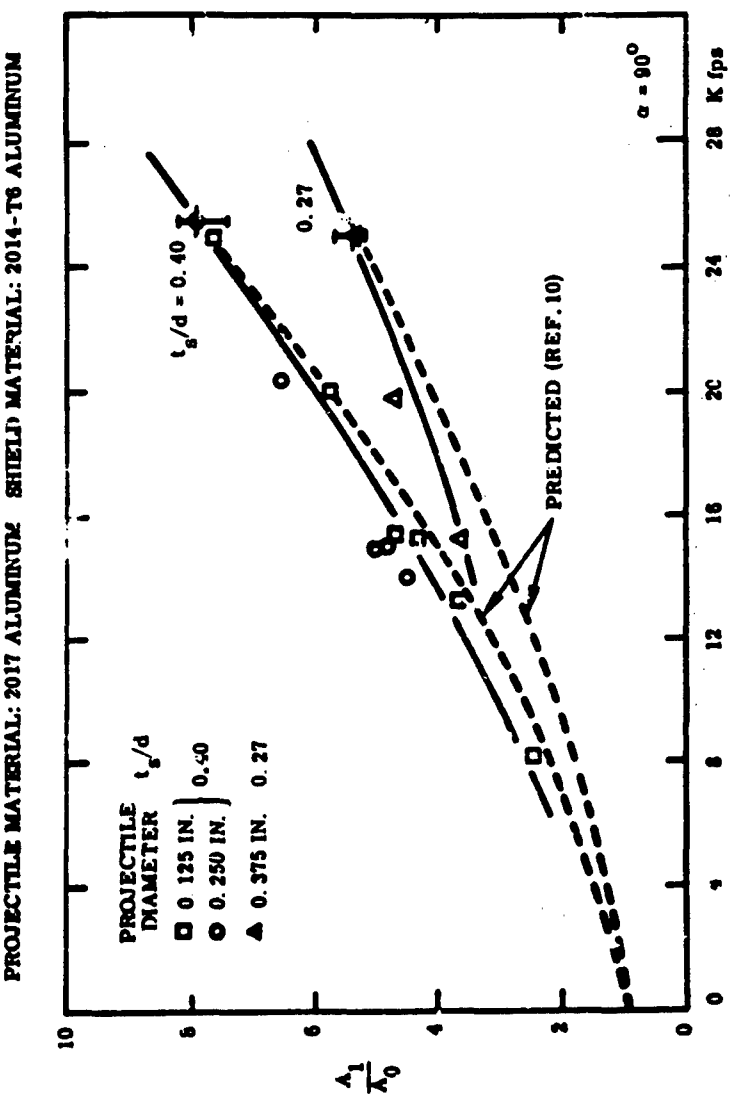

Fig. 12 Shield Damage, $\alpha = 90^{\circ}$, Effect of Variation of Velocity

where

D = hole diameter in shield
d = projectile diameter
v = impact velocity, kfps

The minor differences, especially at the lower velocities, can be attributed to the dissimilarity in materials tested (the empirical formula was derived for shields of 2024-T3 aluminum) and the dearth of data points to determine the experimental scatter, especially for the thinner targets.

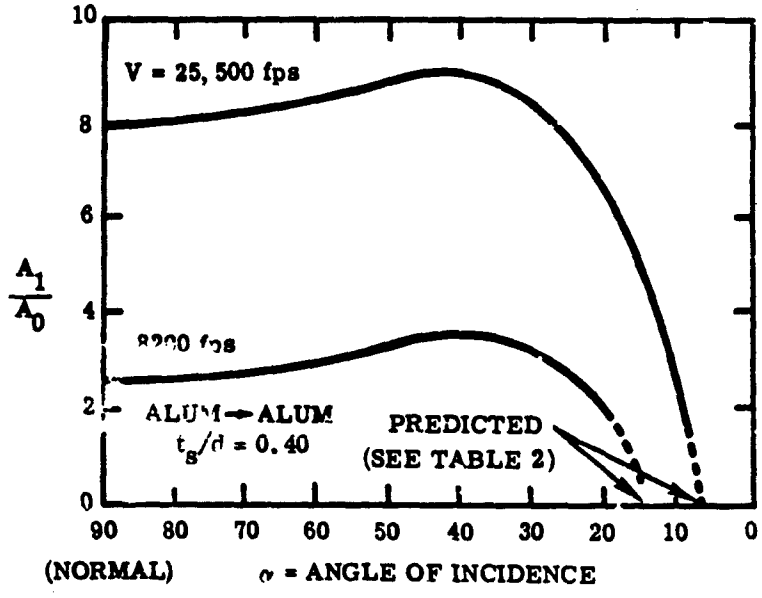

Fig. 13 Shield Damage, Effect of Variation of Velocity, Constant t_s/d

The data in Fig. 13 presents another aspect of shield damage with respect to velocity change. Even though the velocity here has been decreased from 25, 500 fps (data from Fig. 7) to 8200 fps, the characteristic shape of the A_1/A_0-α curve described previously is unaltered except when $\alpha \leq 30^\circ$. In this region the slope of the curve is less steep, and although the shield was perforated when $\alpha = 20^\circ$ it was not perforated when $\alpha = 10^\circ$. There is, then, a shield angle that causes the projectile to ricochet so that perforation does not occur. It is interesting to note the correlation between the observed angular region of ricochet-perforation and that predicted by considering the equivalent semi-infinite target penetration, $(P/d)_{semi\ \infty}$, of the projectile at a given velocity, then applying a thin sheet conversion factor and equating this result $(P/d)_{thin\ target}$, with the apparent thickness of the shield, t_A (t_A is the thickness of the shield measured in the direction of the projectile velocity vector (see Fig. 14)).

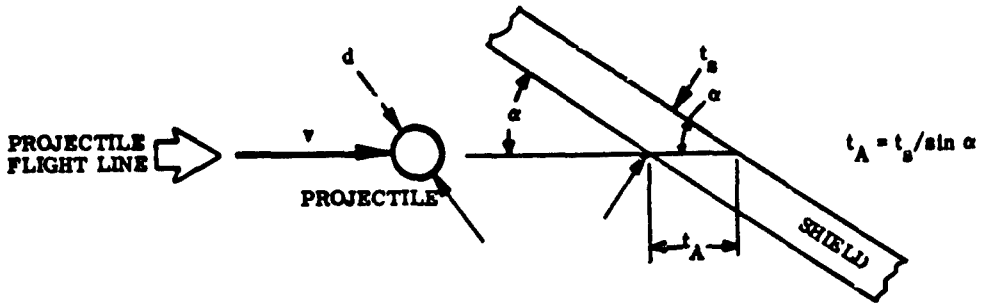

Fig. 14 Schematic of Shield Geometry

Although several empirical relationships are available to compute $(P/d)_{semi\ \infty}$, (Refs. 11, 12, 13) that of Herrmann and Jones has been chosen because of its low-velocity data fit, i.e.,

$$(P/d)_{semi\ \infty} = K_1 (\rho_P/\rho_T)^{2/3} \log_e \left[1 + \left\{ \frac{\rho_T^{2/3} \rho_P^{1/3} v^2}{K_2 BHN} \right\} \right] \quad \text{(Ref. 14)}$$

The relationship for the conversion of semi-infinite target penetrations to those of thin sheets is not well defined, (Refs. 10 – 16) appearing to be a function of projectile and target material as well as velocity. Therefore, the following relationships were chosen as being representative:

$$(P/d)_{thin\ target} = 1.5\ (P/d)_{semi\ \infty} \quad \text{(min)}$$

$$= 2.0\ (P/d)_{semi\ \infty} \quad \text{(max)}$$

As noted, the equating of $(P/d)_{thin\ target}$ to t_A will produce a shield angle below which ricochet occurs and above which perforation occurs. This shield angle is defined as α_1.

The results of this equation are shown in Table 2.

Table 2

RICOCHET-PERFORATION CROSSOVER REGION

PROJECTILE		SHIELD		
d (inches)	v (fps)	t_s (inches)	α_1	
			Experimental	Predicted
0.250	25500	0.100	$\alpha_1 < 10^o$	$5^o < \alpha_1 < 8^o$
0.125	8200	0.050	$10^o < \alpha_1 < 20^o$	$13^o < \alpha_1 < 18^o$
0.375	25100	0.100	$\alpha_1 < 10^o$	$9^o < \alpha_1 < 12^o$

Note: α_1 is the shield angle below which ricochet occurs and above which perforation occurs.

Figures 15 and 16 demonstrate the variation of perforation area with velocity for shield angles of 60 degrees and 25 degrees respectively. For comparison, these graphs are replotted to show variation of perforation with respect to velocity for constant t_s/d; see, for example, Fig. 17a ($t_s/d = 0.27$) and Fig. 17b ($t_s/d = 0.40$). Although normal impacts show an essentially linear variation with velocity, this does not seem to be the case for shield angles other than normal. The perforation area increases with velocity, but the rate of increase decreases with increasing velocity. This rate also seems to be a function of shield angle and thickness. It is interesting to note that for Al → Al impacts, the following variation of Equation (1) represents the hole minor diameter in the region $20^o < \alpha \leq 90^o$:

$$\frac{D_{minor}}{d} = 0.1372\, v \sin\alpha \left\{\frac{t_A}{d}\right\}^{2/3} + 0.90$$

where $t_A = t_s/\sin\alpha$

Although the perforations are elliptical, the hole major diameter is a function of velocity, thickness, and angle; hence no simple adequate expression for actual area can be derived without making gross assumptions. This expression, however, is believed to represent a minimum perforation area and to be especially representative of the damage when $60^o < \alpha \leq 90^o$, for it is in this region that $D_{major} \simeq D_{minor}$.

The properties of projectile and target materials also govern hole size. It has been demonstrated that, all else constant, a decrease in the shield strength will produce a larger hole. (Ref. 16) Other physical property variations have produced indeterminate results and no definite correlations are

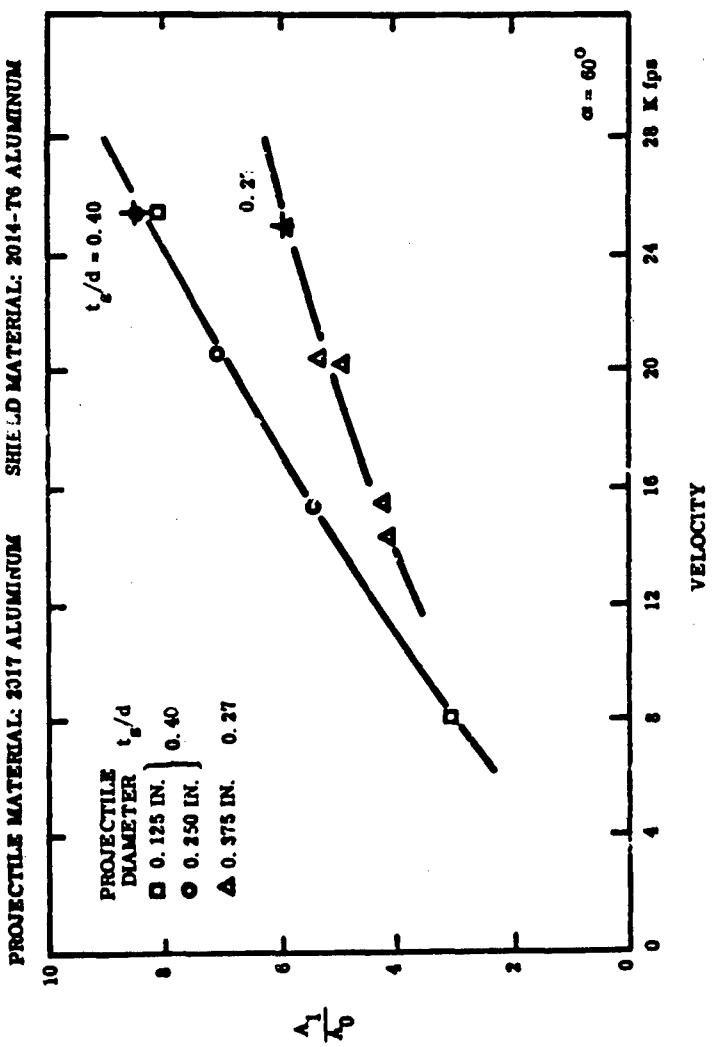

Fig. 15 Shield Damage, $\alpha = 60^\circ$, Effect of Variation of Velocity

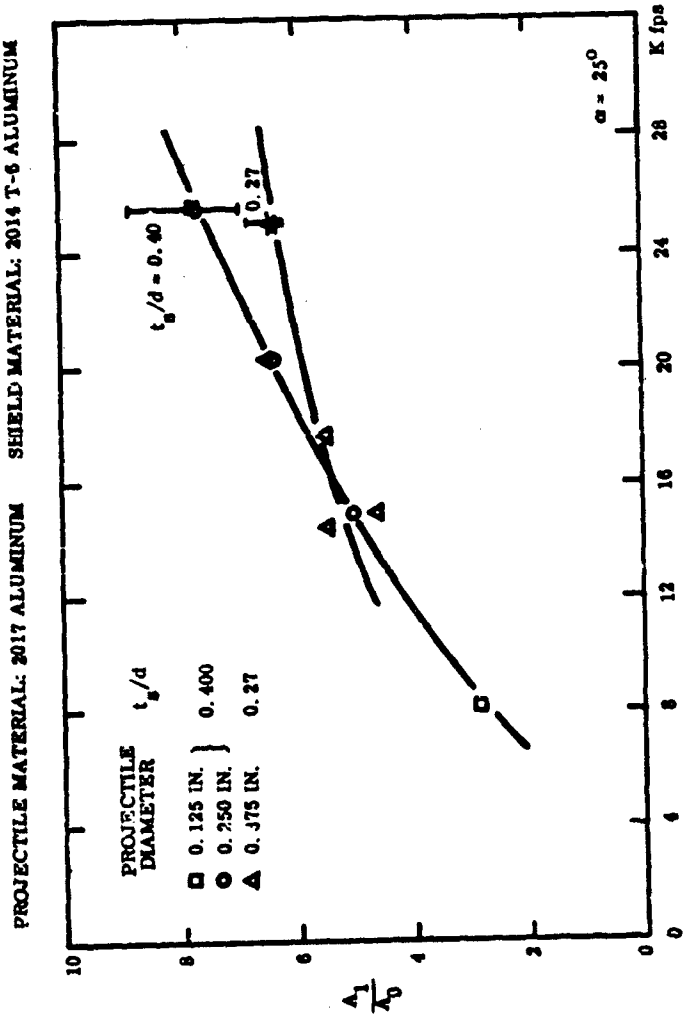

Fig. 16 Shield Damage, $\alpha = 25^{\circ}$, Effect of Variation of Velocity

PROJECTILE MATERIAL: 2017 ALUMINUM SHIELD MATERIAL: 2014-T6 ALUMINUM

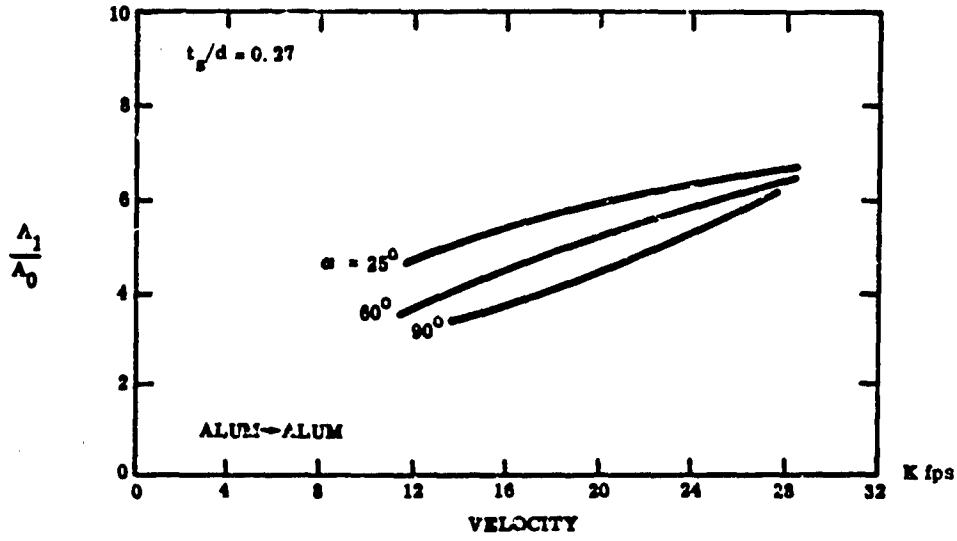

Fig. 17a $t_s/d = 0.27$

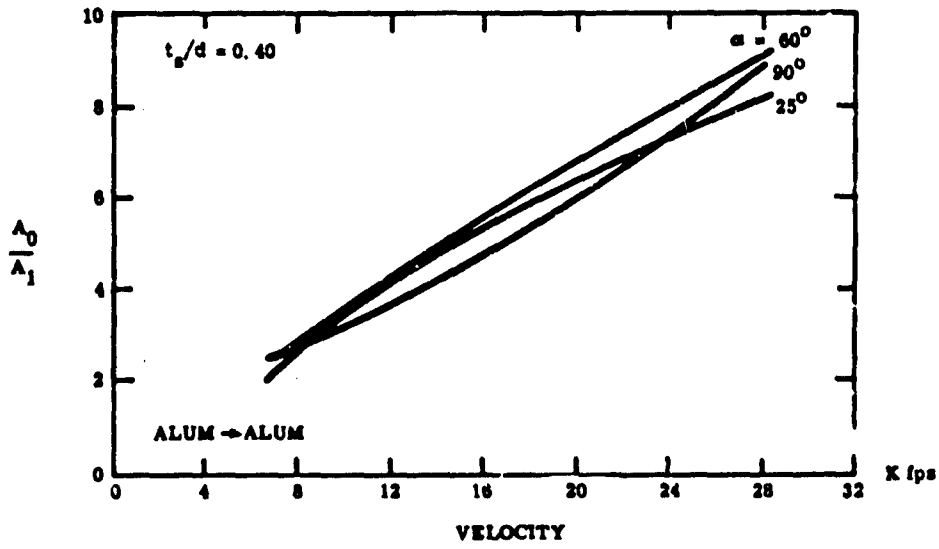

Fig. 17 Shield Damage, Effect of Variation of Velocity, Constant t_s/d

available. However, the changes in hole area resulting from the differences in physical properties appear to be insignificant compared to the changes in hole area resulting from different angles of incidence.

2.4 Target Sheet Analysis

The effect of projectile impact on the shield, or "outer spacecraft shell," has been explored extensively on the preceding pages. The subsequent effects of impact will next be investigated. In certain cases, the second sheet (target sheet) in the analog structure is the main hull – the structural-load-carrying hull. The vulnerability of this sheet, then, is of paramount importance. In review (see Fig. 4), the target sheets for this program have been primarily 0.109-in. 2014-T6 aluminum, except for a short test series with 0.028-in., Type 302 stainless steel targets. The spacing between the target sheet and its shield has been varied from 4 to 24 inches, and the angle of incidence β of the target sheet has been set at 90, 60, and 25 degrees.

The spray patterns obtained from a typical sequence of firings using 2017-aluminum spheres are shown in Fig. 18. The spheres are 3/8 inch in diameter, the spacing between the shield and target along the projectile flight line is 24 inches, and the mean projectile velocity is 25,000 fps.

A review of these targets indicates that an appraisal of the damage potential of the spray is so complicated that a qualitative assessment is required. In order to understand the phenomenon, it is therefore necessary to consider first the simplest case, i.e., normal impact, referring both to the shield ($\alpha = 90^{\circ}$) and to the target sheet ($\beta = 90^{\circ}$) behind the shield.

The phenomena of normal hypervelocity impact has been summarized in Section I, and many authors have presented theories and corroborating experimental evidence (Refs. 9 – 13). Suffice to say, then, that impact velocity, more than any other factor, will affect the target damage resulting from any projectile-shield combination. Typical spray patterns obtained by varying the projectile velocity are shown in Fig. 19. These experiments at different velocities illustrate two important results.

(1) Increased velocity results in more complete fragmentation of both projectile and shield.

X-rays of impact show that at low velocities the projectile suffers very little damage during perforation (see Fig. 19), and that only sparse, large, irregular fragments emanate from the shield. At 25,000 fps, however, the spray particles emitted from the back of the shield are so minute and diverse that they are difficult to distinguish from the background of the radiograph.

PROJECTILE MATERIAL: 2017 ALUMINUM
DIAMETER: 0.312 in.
VELOCITY: > 25,000 fps

SHIELD / TARGET | MATERIAL: 2014-T6 ALUMINUM
THICKNESS: 0.100 in.
SPACING: 24 in.

TARGET ANGLE OF INCIDENCE – β

SHIELD ANGLE OF INCIDENCE – α

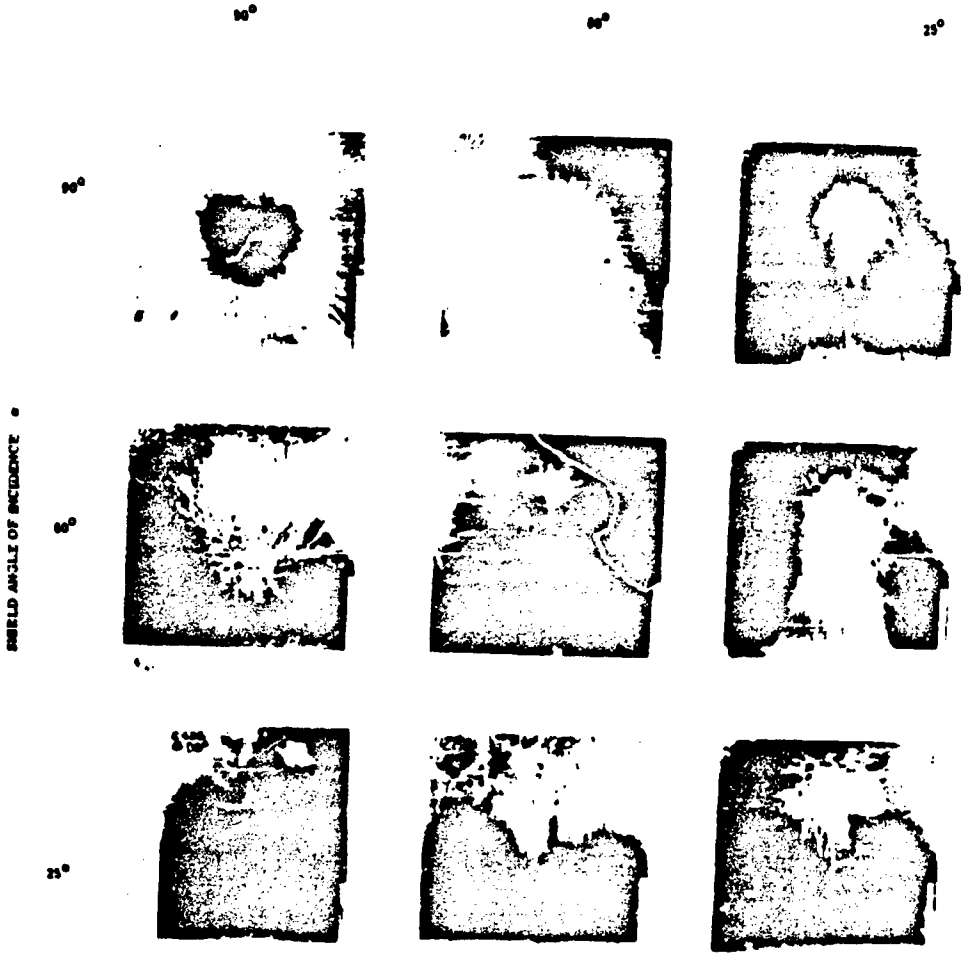

NOTE: TARGET IN LOWER LEFT CORNER IS 36" x 54". ALL OTHER TARGETS SHOWN ABOVE ARE 36" x 36"

Fig. 18 Typical Target Spray Patterns (Shields removed), Al → Al

PROJECTILE MATERIAL: 2017 ALUMINUM SHIELD MATERIAL: 2024-T6 ALUMINUM

SHIELD TO TARGET SPACING = 12 INCHES

t_s/d = 0.40	0.27	0.27	0.27
d = 0.125 IN	0.375 IN	0.375 IN.	0.375 IN

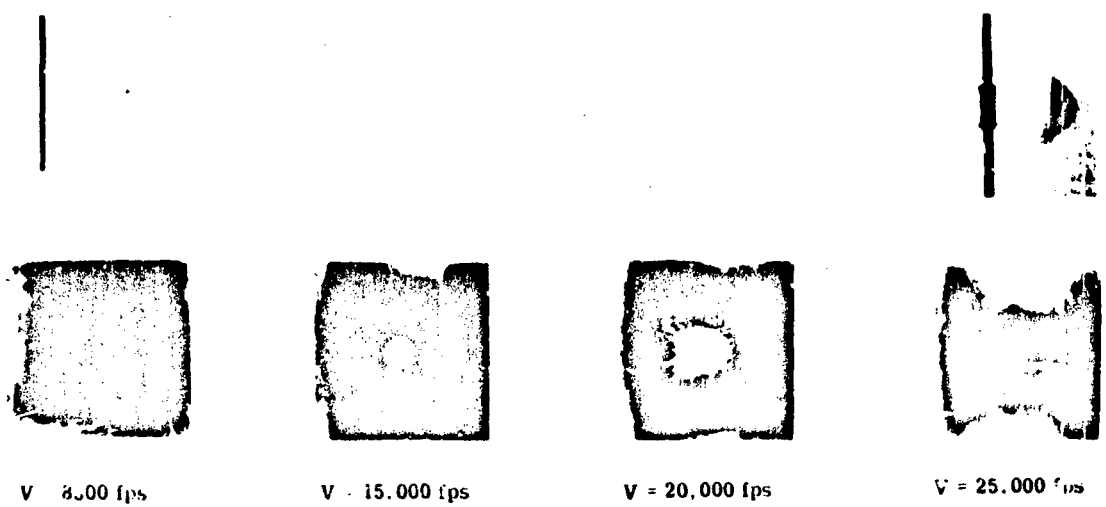

V = 8,500 fps V = 15,000 fps V = 20,000 fps V = 25,000 fps

Fig. 19 Typical Target Spray Patterns – Effect of Variation of Velocity

CONFIDENTIAL

(2) Increased velocity results in a greater dispersal of both projectile and shield fragments.

This result can also be seen in Fig. 19. With each increase in velocity (intersheet spacing constant), a greater target sheet area is affected. This effect of velocity on projectile-shield fragment dispersal is also shown graphically (Fig. 20) for Al – Al impacts by plotting projectile- and spall-spray semi-angles for two combinations of projectile and shield. The projectile-spray semi-angle γ is defined here as

$$\gamma = \tan^{-1} \frac{D_p}{2S}$$

where D_p is relevant diameter of damage on the target sheet, and S is intersheet spacing between shield and target, measured along the projectile flight line. The spall-spray semi-angle θ is

$$\theta = \tan^{-1} \frac{D_S}{2N}$$

where D_S is relevant damaged diameter centered at the point where a normal drawn from the point of impact on the shield intersects the target, and N is the length of the appropriate perpendicular (in this case where $\alpha = \beta = 90^\circ$, N = S). Figures 18 and 19, however, show that it is difficult to define a meaningful diameter of damage, and that physical limitations preclude the inclusion of all spall fragments. As a result, the criterion that was chosen provided that approximately 90 percent of the spall damage to the target should fall within the chosen diameter. A typical target with appropriate measurements is shown in Fig. 21.

In addition to demonstrating that fragment dispersion increases with increasing velocity, Fig. 20 shows effects of sheet thickness (t_s/d) on dispersion angles. It can be seen that at high velocities the spall-spray from the thinner target is more concentrated about the flight line, and the maximum dispersion angle is smaller. The projectile-spray angle appears to be independent of such small changes in t_s/d.

An interesting side note is provided by Fig. 22, in which the angles γ and θ are superimposed on a radiograph of a projectile-shield combination 10 μsec after impact.

It has been shown that the spray emitted from the rear of the shield at normal incidence is symmetric about the original projectile flight line. Under conditions of oblique impact, however, the spray distribution is deflected from the flight line towards the normal through the center of the perforation. The spray seems to be composed of two patterns:

PROJECTILE MATERIAL: 2017 ALUMINUM SHIELD MATERIAL: 2014-T6 ALUMINUM

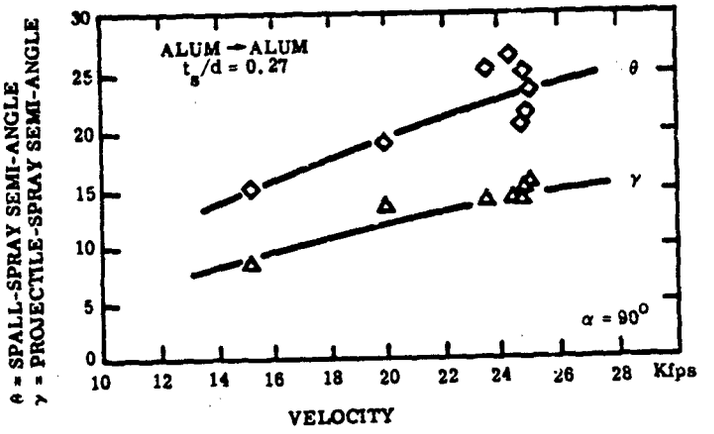

Fig. 20a $t_s/d = 0.27$

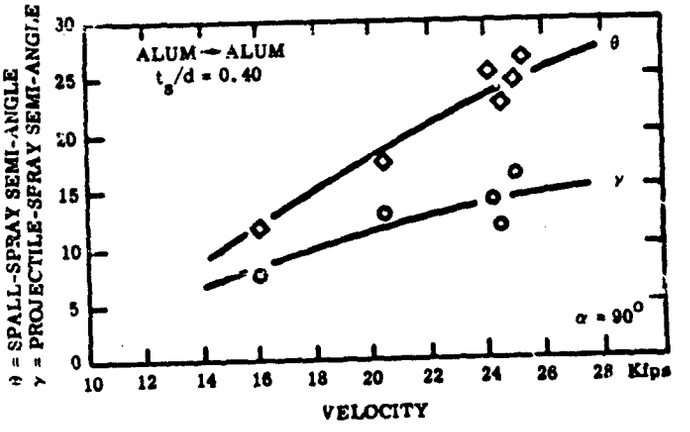

Fig. 20b $t_s/d = 0.40$

Fig. 20 Spall and Projectile Spray Angle Variation with Velocity ($\alpha = 90^o$)

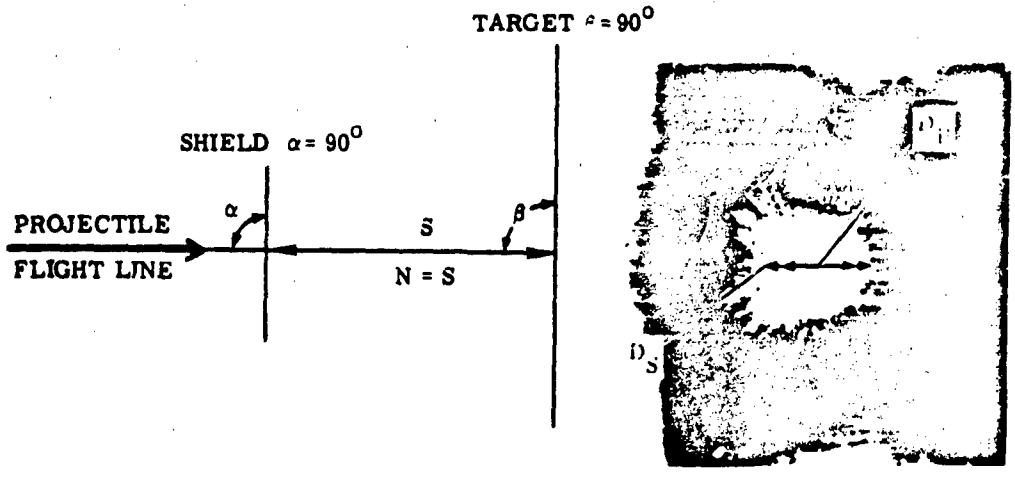

SHIELD AND TARGET SHEET LAYOUT SIDE VIEW – SCHEMATIC (REF. FIG. 4)

TARGET SHEET (SHIELD REMOVED) FRONT VIEW – ACTUAL (REF. FIG. 19)

Fig. 21 Analysis of Spall and Projectile Spray Angles

PROJECTILE MATERIAL: 2017 ALUMINUM SHIELD MATERIAL: 2014-T6 ALUMINUM

DIAMETER: 0.375 IN. t_s/d : 0.27

VELOCITY: 23,500 fps

θ : 25° γ : 14° (REF. FIG. 20a)

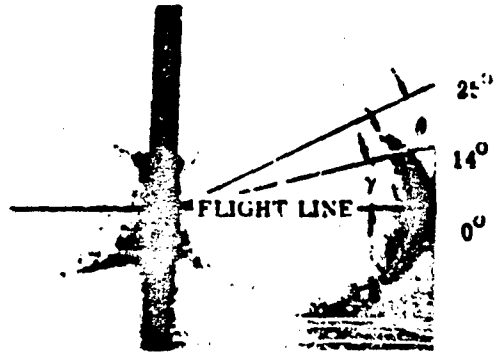

Fig. 22 Superposition of Spray Angles on Typical X-Ray of Projectile-Shield Impact

(1) Fragments distributed about a normal through the shield (probably resulting from shock propagation through the target, i.e., target spall)

(2) Fragments distributed about the original projectile flight line (composed mainly of projectile fragments)

The radiographs shown in Fig. 23 illustrate this point. The normal configuration is the same one noted earlier. In this case, the projectile is completely pulverized and spread over so large a surface that it is difficult to distinguish between damage from the projectile and damage from spall fragments. As the shield incident angle α decreases, however, the obliquity or incident angle effect becomes more apparent. Thus, at $\alpha = \beta = 60^{\circ}$ the two patterns are easily discernible and it can be seen that the spall-spray angle θ has decreased. At $\alpha = \beta = 25^{\circ}$ the target has nearly defeated the projectile (note the minor damage on the plane of the projectile flight line), and the severe target damage has been caused by the large, irregular pieces of spall ejected normally from the shield surface. These observations have been plotted as $\gamma - \alpha$ and $\theta - \alpha$ for two combinations of projectile and shield (Figs. 24 and 25). In both cases it is apparent that as α is decreased, the target sheets are subjected to spall-spray damage long after the hazard from projectile-spray has ceased.

Superimposed on the spall-spray curves are the lower limit predictions ($\theta = 0$) found in Table 2. These predictions seem to be in good agreement with the trend of the curves, but further testing will be required to obtain a velocity-dependent T^*/P for 2014-T6 aluminum that may exceed the assumed value of 2.0. (Note: T^* = maximum thickness of target for complete penetration, and P = crater depth of semi-infinite target.)

The lower limit of the projectile-spray curve ($\gamma = 0$) can be predicted by the expression,

$$t_A = d\sqrt{\rho_P/\rho_T} \quad \text{where} \quad t_A = t_s/\sin\alpha^* \qquad \text{(Ref. 15)}$$

This simple variation of the proven expression of primary penetration depth (Ref. 15) defines an angle α^* below which there will be no damage from in-line spray particles, i.e., no target damage in the direction of the projectile flight line. Typical values of α^* are shown in Table 3.

PROJECTILE MATERIAL: 2017 ALUMINUM
DIAMETER: 0.375 IN.
VELOCITY: 25,000 fps

SHIELD TARGET MATERIAL: 2014-T6 ALUMINUM
t_s/d : 0.27
SPACING: 12 INCHES

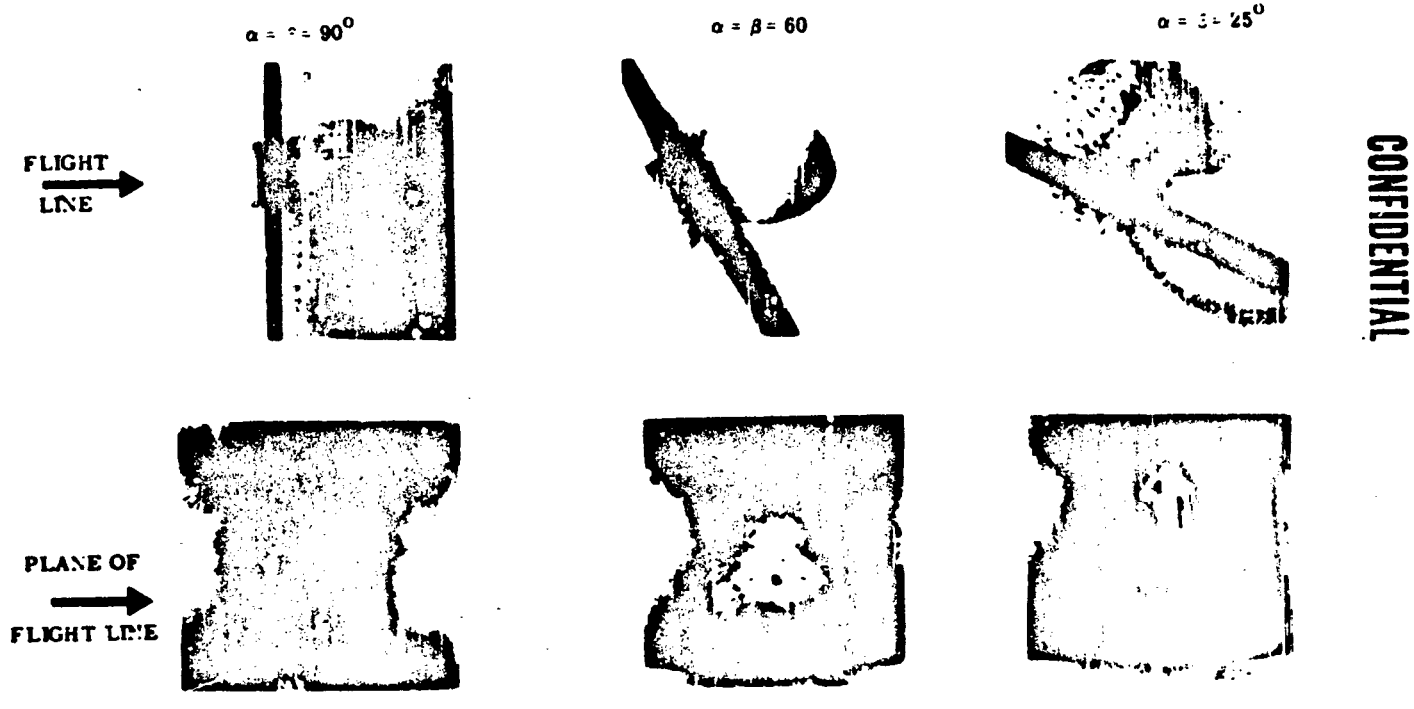

Fig. 23 Typical Target Patterns – Effect of Variation of Shield Angle

PROJECTILE MATERIAL: 2017 ALUMINUM
DIAMETER: 0.375 IN
VELOCITY: 25000 fps

SHIELD MATERIAL: 2014-T6 ALUMINUM
t_s/d : 0.27

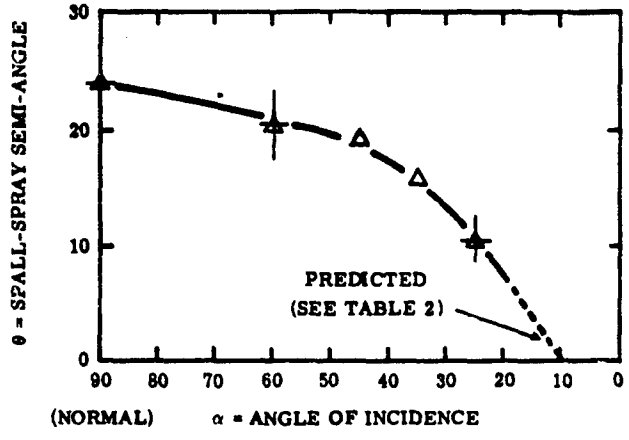

Fig. 24a Spall-Spray Semi-Angle

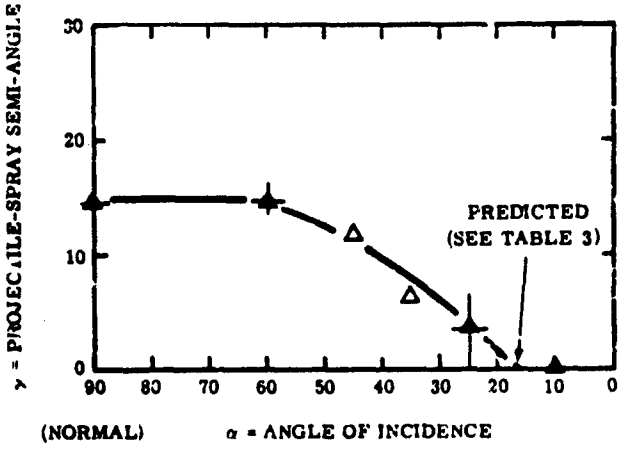

Fig. 24b Projectile-Spray Semi-Angle

Fig. 24 Spall and Projectile Spray Angle Variation with Shield Angle – Al → Al (t_s/d = 0.27)

PROJECTILE MATERIAL: 2017 ALUMINUM SHIELD MATERIAL: 2014-T6 ALUMINUM
DIAMETER: 0.25 IN t_s/d : 0.40
VELOCITY: 25,500 fps

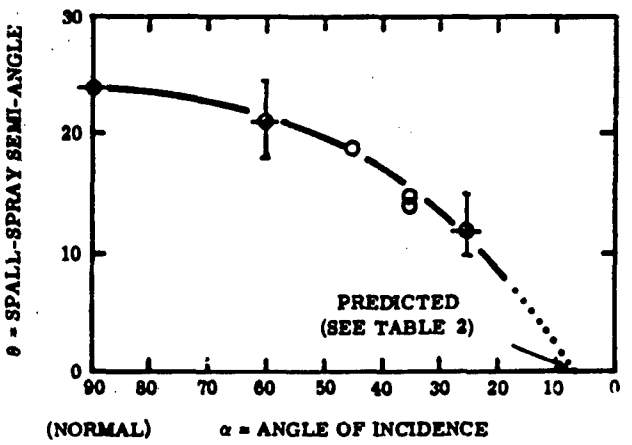

Fig. 25a Spall-Spray Semi-Angle

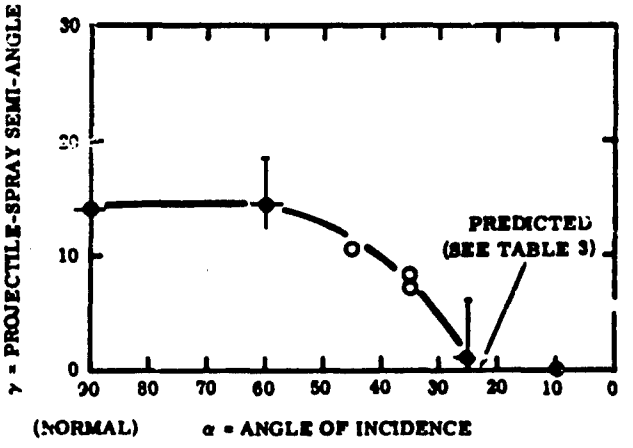

Fig. 25b Projectile-Spray Semi-Angle

Fig. 25 Spall and Projectile Spray Angle Variation with Shield Angle – Al – Al (t_s/d = 0.40)

Table 3

LIMITING SHIELD ANGLE TO PREVENT PROJECTILE SPRAY DAMAGE

ρ_P (gm/cc)	ρ_T (gm/cc)	t_s/d	α^*	
			Experimental	Predicted
2.70	2.70	0.27	16^o (Fig. 24)	15.5^o
2.70	2.70	0.40	24^o (Fig. 25)	23.6^o
19.1	1.77	0.70	$12^o < \alpha^* < 15^o$ (6)	12.3^o
8.90	2.70	0.534	-	17.2^o
8.90	8.1	0.15	-	8.2^o

The lack of data precludes experimental predictions of α_1 and α^* for impacts of Ni - Al and Ni - stainless steel; although no data has been plotted, selected points are included in Appendix I.

Figure 26 illustrates the variation with velocity of spall-spray and projectile-spray angles when $\alpha = 60^o$. The curve trends shown here are similar to those of Fig. 20 for $\alpha = 90^o$; hence, the conclusions are the same. Insufficient data prevents comment on velocity variation when $\alpha = 25^o$.

2.5 Total Target Vulnerability

The purpose of these tests is to define the vulnerability of the total structure, or system, under set conditions of projectile impact. There is, therefore, an interest in total penetration, because penetration is indicative of (1) the ability of a shield to fragment the projectile, to spread these fragments and reduce their velocities, and (2) the ability of the target sheet to resist these fragments.

Material considerations aside, total penetration is primarily a function of sheet thickness, projectile velocity, and intersheet spacing. (For this report, only total penetrations when $\alpha = \beta = 90^o$ have been plotted. Target damage is shown both pictorially (Fig. 27) and graphically (Fig. 28).) When intersheet spacing is small, target failure takes the form of perforation by projectile and spall fragments, and petalling from the high impulse loads. As the spacing is increased, neither perforation nor petalling occurs. Note that at larger spacings the target sheet is vulnerable to the projectile of greater mass, e.g., when $t_s/d = 0.27$ and $t_s = 0.100$ in. (Fig. 27).

PROJECTILE MATERIAL: 2017 ALUMINUM SHIELD MATERIAL: 2014-T6 ALUMINUM

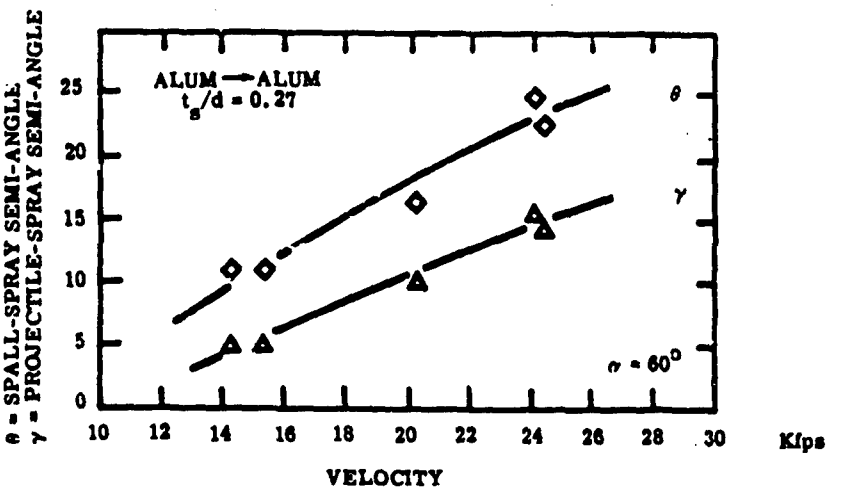

Fig. 26a $t_s/d = 0.27$

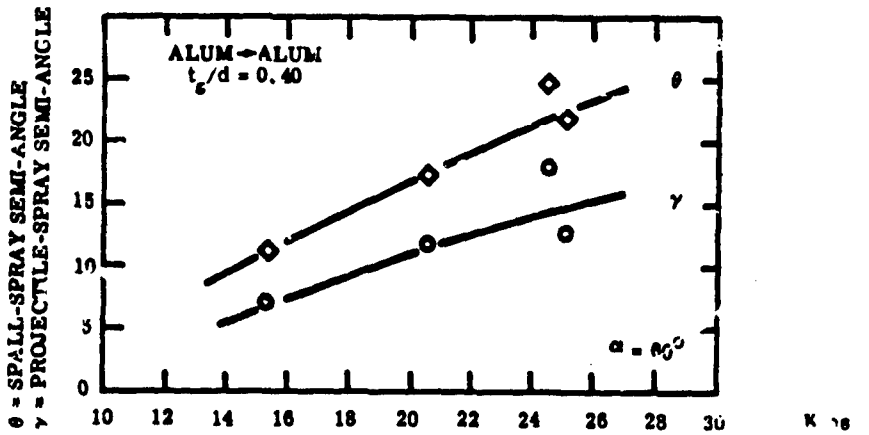

Fig. 26b $t_s/d = 0.40$

Fig. 26 Spall and Projectile Spray Angle Variation with Velocity ($\alpha = 60^{\circ}$)

PROJECTILE MATERIAL: 2017 ALUMINUM
DIAMETER: 0.375 IN.
VELOCITY: 25,000 fps

SHIELD } MATERIAL: 2014-T6 ALUMINUM
TARGET }

$\alpha = \beta = 90^{\circ}$

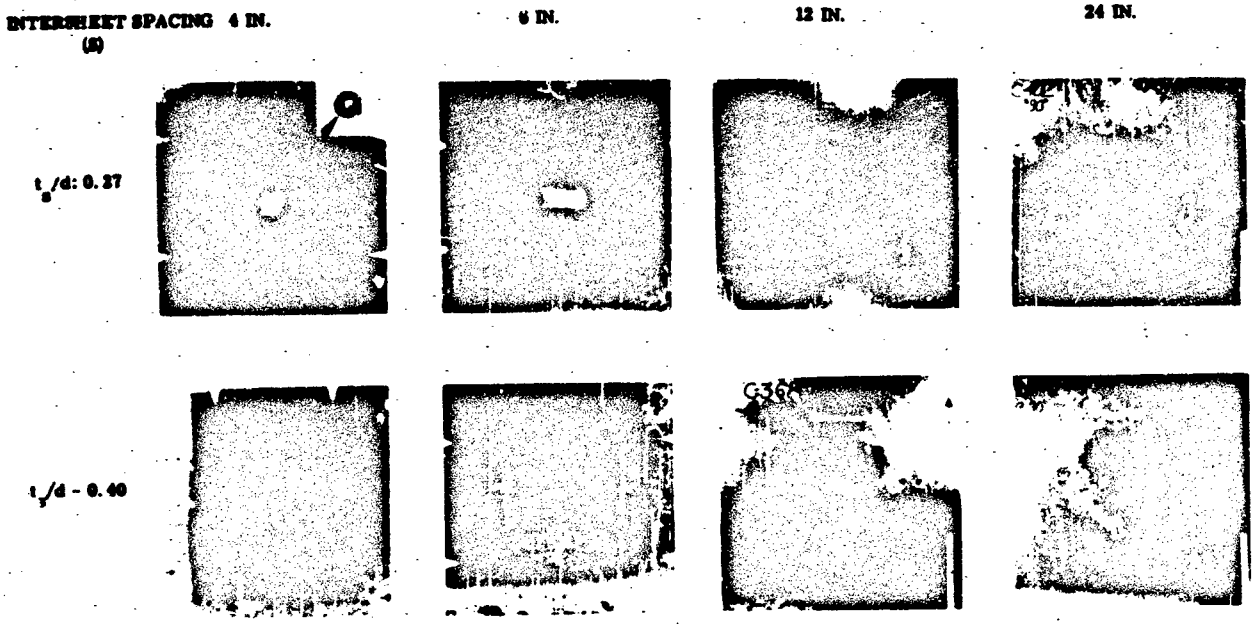

TARGET SHEETS WHERE S = 4 AND S = 6 ARE 18 IN. x 18 IN.; OTHERS SHOWN ARE 36 IN. x 36 IN.

Fig. 27 Typical Target Patterns – Effect of Variation of Intersheet Spacing

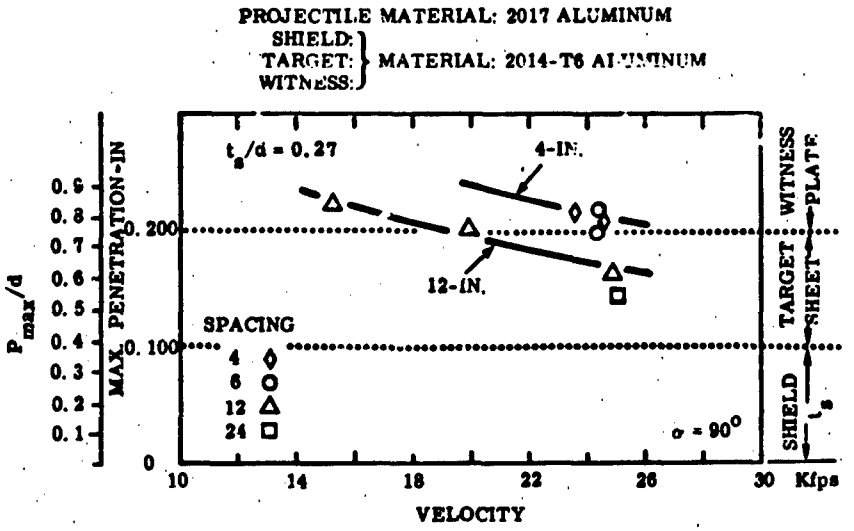

Fig. 28a $t_s/d = 0.27$

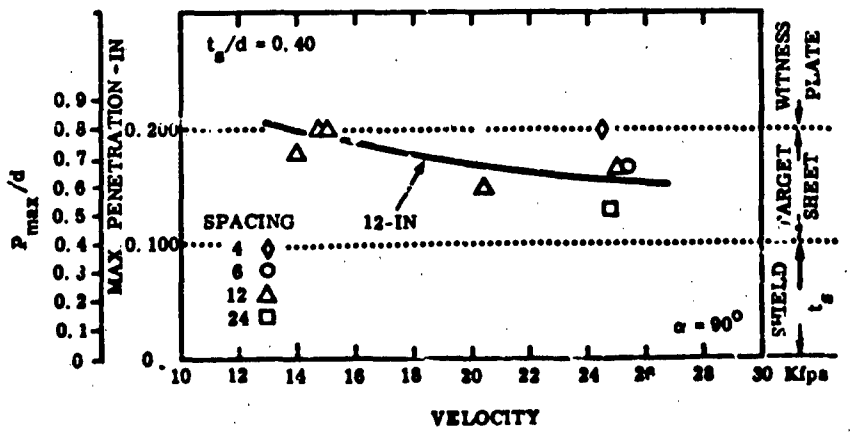

Fig. 28b $t_s/d = 0.40$

Fig. 28 Effect of Velocity on Maximum Penetration – Al → Al ($\alpha = 90^o$)

To present an overall picture of the vulnerability of the aluminum analog structures, a ballistic limit approach has been chosen: either perforation or no perforation of the target sheet. Spacings of both 12 and 24 inches have been considered, along with the surmised cause of damage – either projectile fragments or spall. This data is presented in Figs. 29 and 30, which show that as the shield and target impact angles are varied, target sheet failure results from different mechanisms. However, it can be seen that the resultant damage of any configuration is governed primarily by the shield angle α. Since the results for all four cases are similar, discussion is limited to the case where $t_s = 0.27$ and intersheet spacing = 12 inches. Under conditions of normal impact, no perforations from either projectile fragments or spall occurred, although the target sheet from the $\alpha = \beta = 90^\circ$ impact appeared in danger of rupture from projectile-fragment and spall-fragment momentum loading. When $\alpha = 60^\circ$ no perforations resulted from spall, although the projectile fragments perforated when $\beta = 60^\circ$ and 90°. It is felt that the extreme obliquity of the target sheet when $\beta = 25^\circ$ defeated these fragments. When $\alpha = 25^\circ$ the major damage to the target sheets resulted from the irregular spall fragments ejected from the shield; these perforated the target sheet under all conditions. Again, when $\beta = 25^\circ$ the angle of obliquity of the target sheet was sufficient to defeat the projectile fragments.

With the 0.3-gm 2017 aluminum projectiles and the 0.100-inch 2014-T6 aluminum shield and target as references, two series of tests involving nickel spheres of equivalent mass and Type 302 stainless steel shields and targets of equivalent strength were conducted. Typical results are shown pictorially in Fig. 31 and numerically in Appendix I. It can be seen that in all cases the nickel projectiles are more lethal than the aluminum. A review of the witness sheet penetrations indicates that the stainless steel analog structure is generally less vulnerable than the aluminum when impacted by nickel projectiles. However, a larger sample of materials should be tested before any conclusions are drawn regarding projectile and shield-target physical properties.

2.6 Impact Flash Phenomenon

An investigation of the phenomenon of impact flash was made along with the hypervelocity impact study. This investigation was to qualitatively determine the pertinent variables affecting impact flash with the ultimate goal of using the information to assess the impact flash phenomenon as a spatial hit detector or target discriminator. Although open-shutter and high-speed framing cameras have provided results concerning total radiant energy and flash duration (Fig. 32), more precise empirical data will be required for the above application. Pursuant to this, a series of photomultiplier detectors, sensitive to visible and near-visible radiation, were chosen for a parametric investigation. (See Section 2.1 for instrumentation details.) During this study, only the peak luminosity I_p displayed on the typical oscilloscope trace (Fig. 32) has been correlated (I_p is defined as the maximum

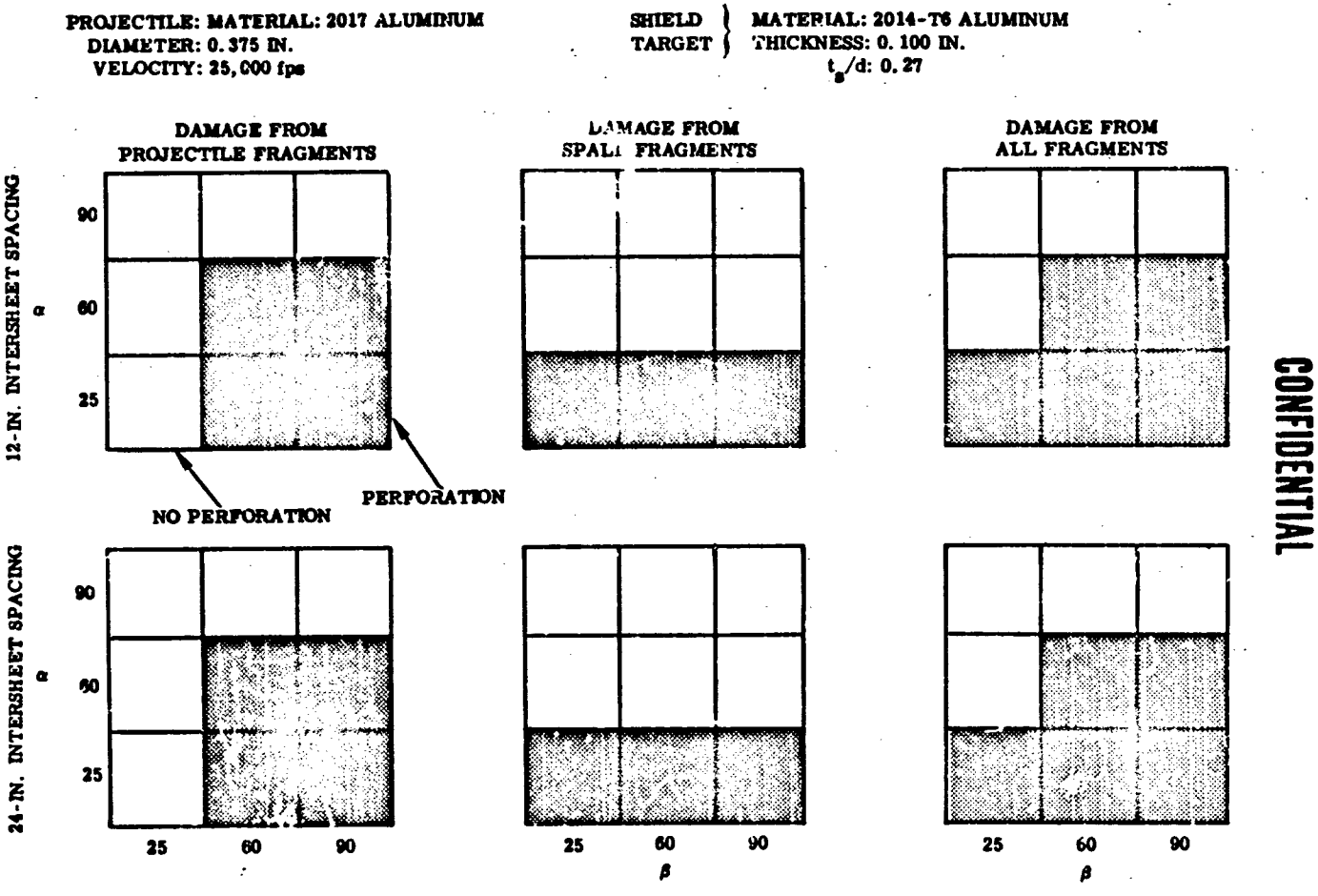

Fig. 29 Vulnerability of Multisheet Thin Target Assembly, Al → Al (t_s/d = 0.27, v = 25,000 fps)

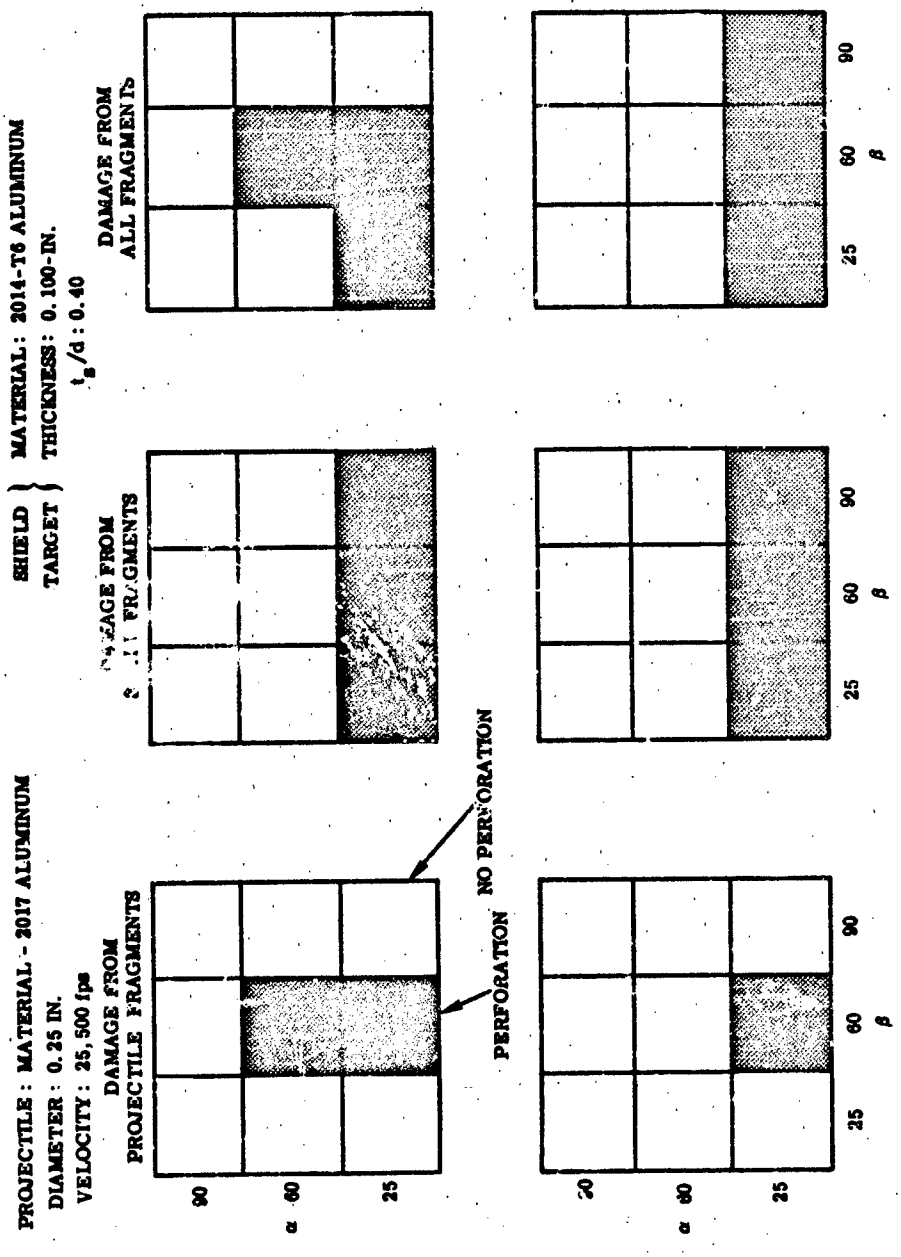

Fig. 30 Vulnerability of Multisheet Thin Target Assembly, Al → Al (t_s/d = 0.40, v = 25,000 fps)

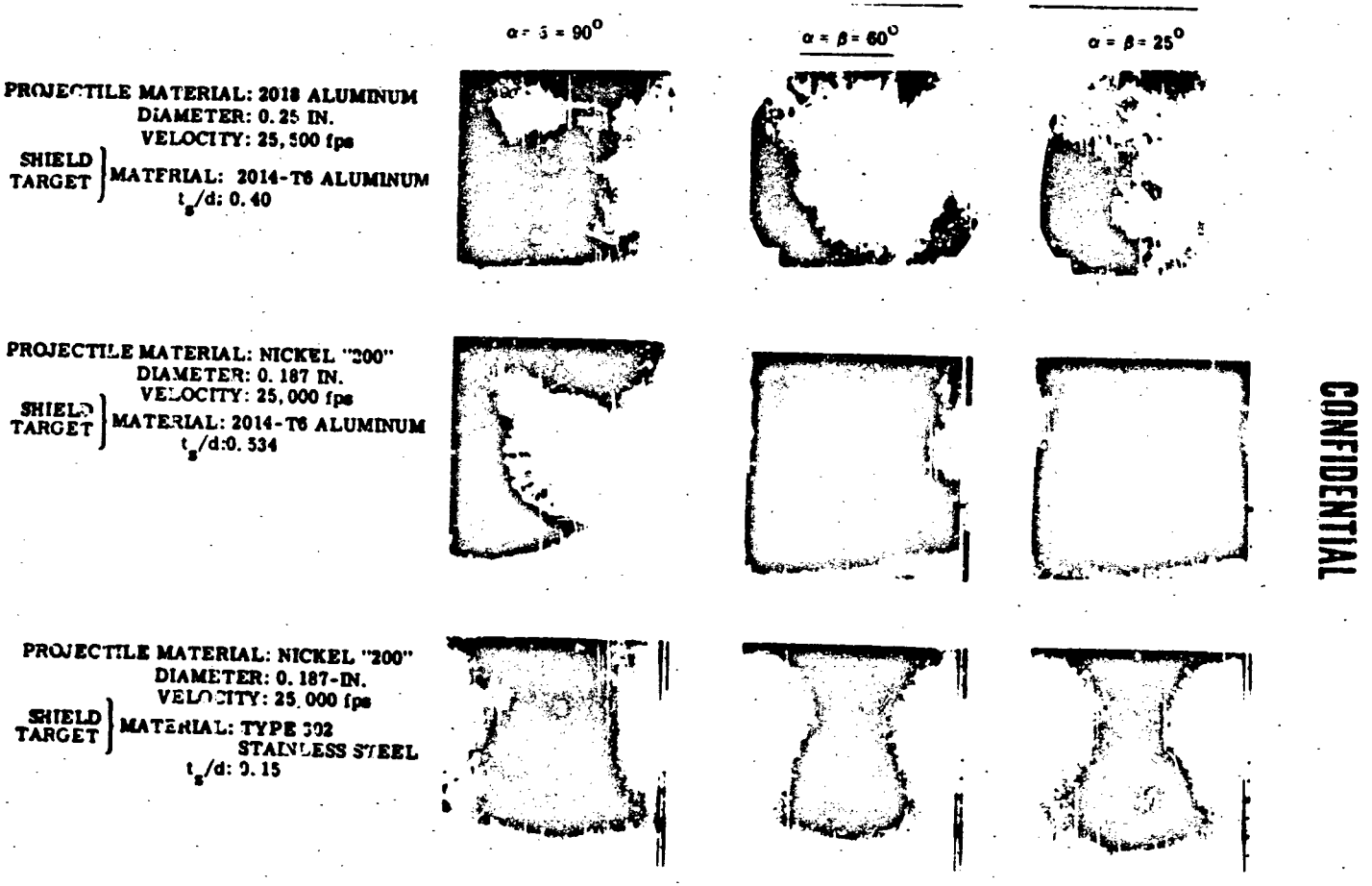

Fig. 31 Typical Target Patterns – Effect of Varied Projectile and Target Assembly Materials

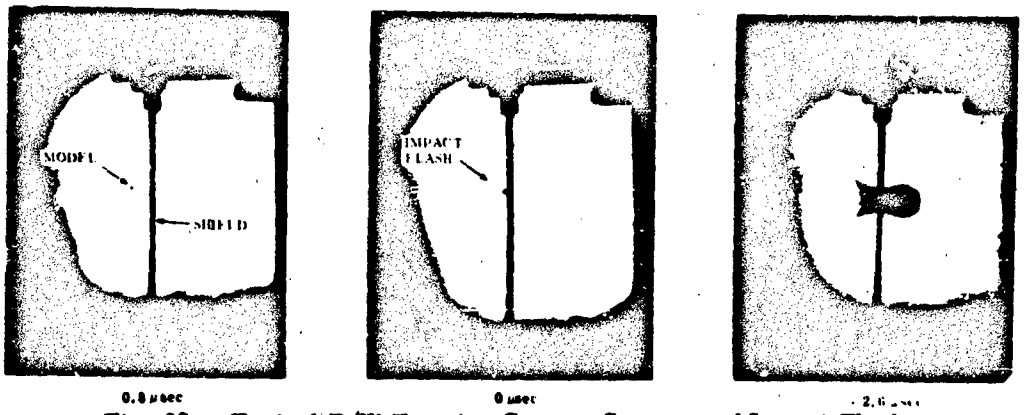

Fig. 32a Typical B/W Framing Camera Sequence of Impact Flash

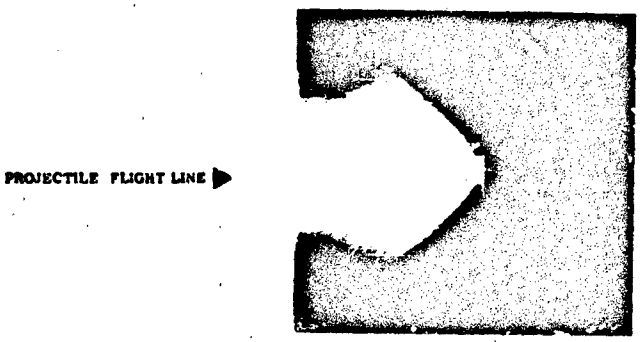

Fig. 32b Typical Open-Shutter Camera Photograph of Impact Flash

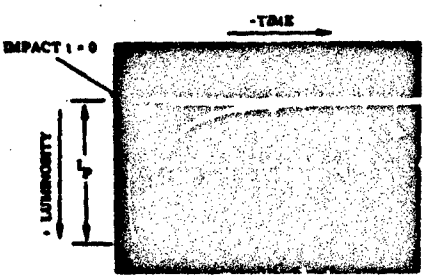

Fig. 32c Typical Oscilloscope Trace Showing Intensity-Time History of Impact Flash

recorded luminosity occurring within the first few microseconds after contact of the projectile with the shield and before any possible interference effects from spall splatter on the target sheet or on the walls of the impact chamber).

Again, since one of the projected uses of the impact flash phenomenon is that of a spatial hit detector or target discriminator, obviously the existence of impact flash under environmental conditions of reduced gas pressure must be proved. To this end, experiments involving Al → Al impacts were conducted in reduced atmospheres of air and helium (the helium simulates an inert atmosphere). It can be seen in Fig. 33, for V-constant, that the peak luminosity is essentially invariant in an inert atmosphere and also that only above 1 torr (mm of Hg) is the surrounding air observed to have any significant effect.

To determine the relationship of the impact flash to the many possible projectile parameters, experiments were conducted in which size and velocity of the projectile varied. Projectile and target materials were limited to those discussed earlier – 2017 Al for the projectile and 2014-T6 Al for the target. Three independent tubes monitored tests with projectiles 0.125 inch in diameter to determine any dependence of frequency response to velocity. (See Fig. 34.) Plotted log-log, the peak luminosity is shown to vary as the fourth power of velocity, a relationship independent of the monitored frequency. When data obtained from larger projectiles (0.25 inch and 0.375 inch) was compared to that from the 0.125-inch projectile impacts, the impact flash intensity was found to be a direct function of the area presented by the projectile.

These experimental results confirmed that the following empirical relationship, generated from tests on semi-infinite targets, can be applied to thin sheet impacts under conditions of normal impact.

$$I_{np} = CAv^n \qquad \text{(Ref. 17)}$$

where
- I_{np} = peak luminosity (see definition), normal impact
- A = cross-sectional area of projectile
- v = projectile velocity, fps
- n = velocity exponent
- C = a constant

Within the scope of the experiments conducted, measured values for the coefficient C are listed in Table 3 for Al → Al impacts.

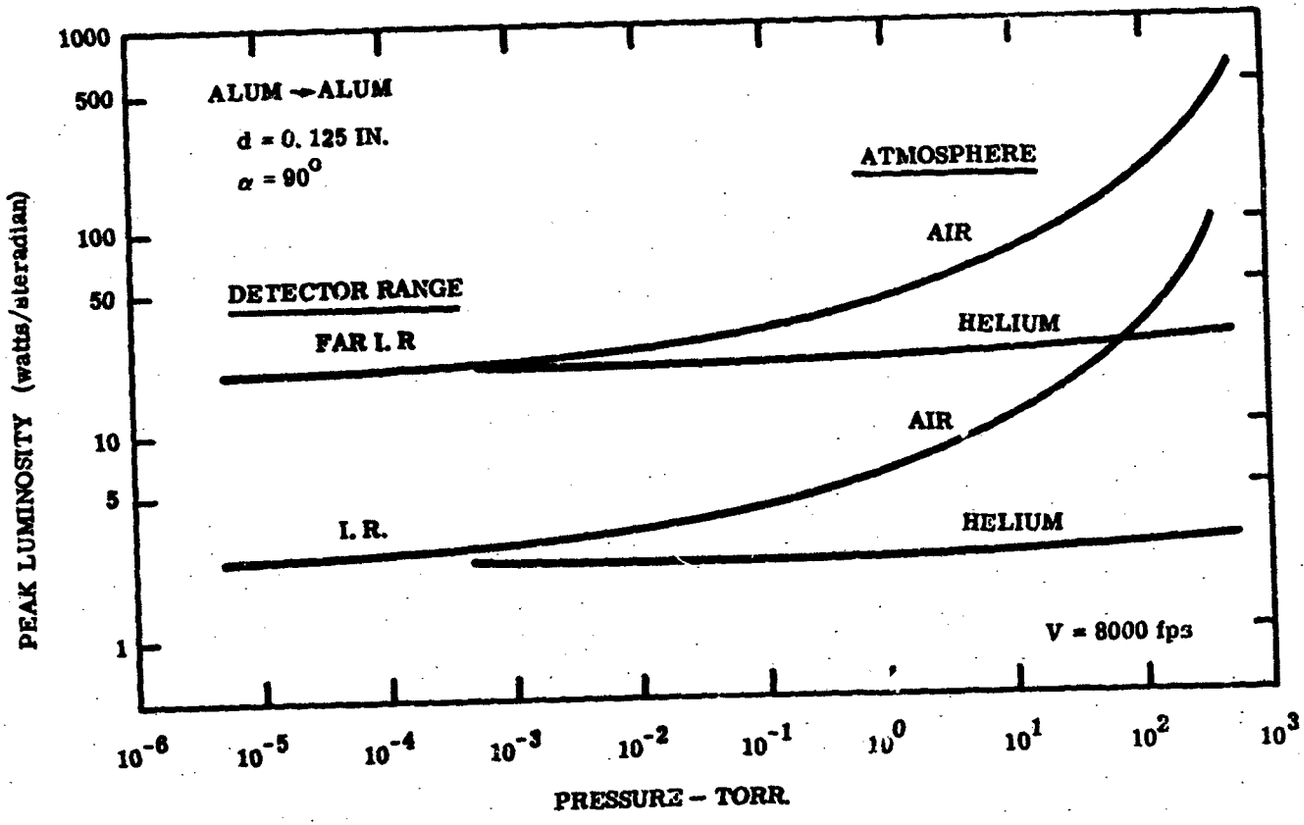

Fig. 33 Reduced Data – Air and Helium Atmospheres – Variation of Peak Luminosity with Range Pressures, Velocity Constant

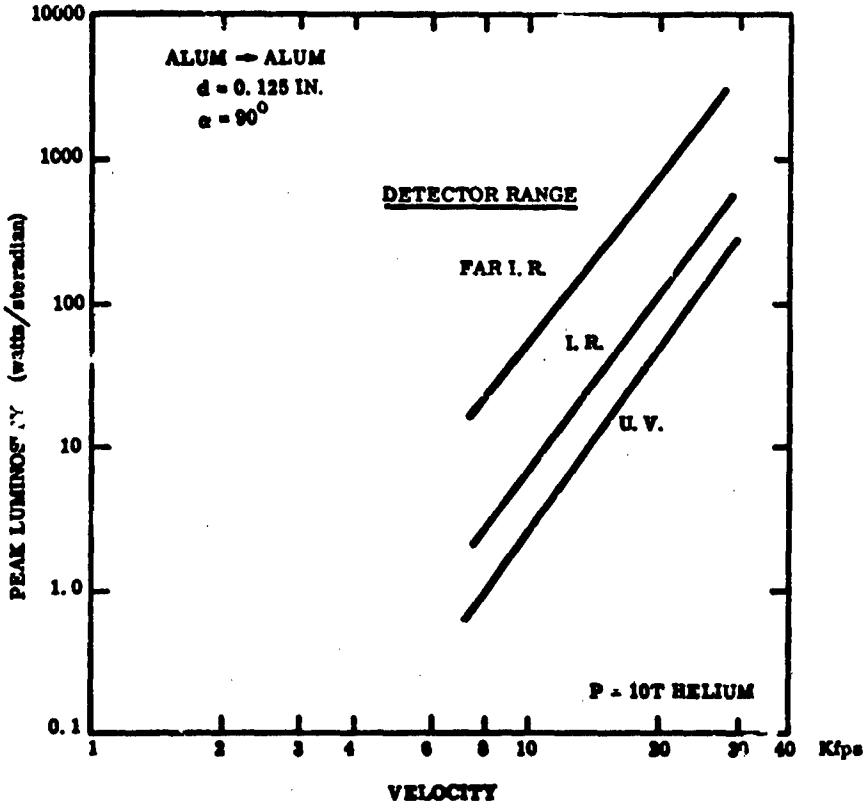

Fig. 34 Variation of Peak Luminosity with Velocity

Table 3

$I_{np} = CAv^n$

VALUES OF TERMS FOR Al → Al IMPACTS

DETECTOR RANGE	n	C
0.18μ to 0.55μ	4.2	5.24×10^{-13}
0.594μ to 1.0μ	4.1	3.27×10^{-12}
1.0μ to 5.5μ	3.9	1.66×10^{-10}

Note: units of C – watts per steradian/ft^2 $(fps)^n$

To appraise the effect of target incidence on peak luminosity, two series of tests were fired – one with semi-infinite targets, and the other with thin targets (Fig. 35). Within the limits of the data scatter, no differentiation can be made between the two sets of results. Furthermore, although data trends are indicated at v = 9,000 fps, there seems to be little variation in the peak luminosity (less than one order of magnitude) over the range of tested incident angles. Data from impacts at v = 25,000 fps confirms the velocity-power relationship over the range of tested incident angles.

PROJECTILE MATERIAL: 2017 ALUMINUM SHIELD MATERIAL: 2014-T6 ALUMINUM
DIAMETER: 0.125 IN.

P: 10T HELIUM

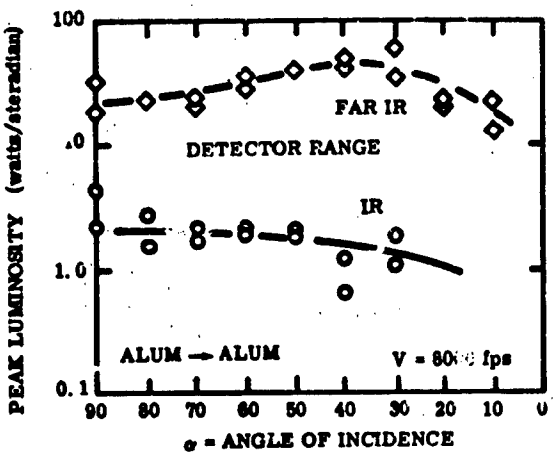

Fig. 35a Semi-Infinite Targets

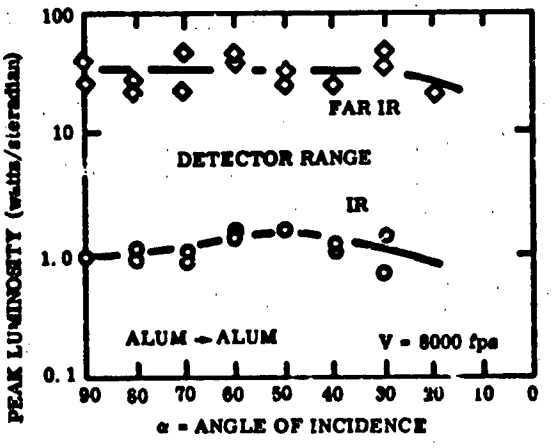

Fig. 35b Thin Targets – $t_3/d = 0.40$

Fig. 35 Reduced Data – Variation of Peak Luminosity with Shield Angle (Semi-Infinite and Thin Targets)

(This page is intentionally blank)

SECTION III
SUMMARY

In summary, the data has covered a range of incident angles from 2 to 90 degrees with various projectile-target combinations. Impact velocities have ranged from 8,000 to 25,600 fps, and shield-to-target spacings have varied from 4 to 24 inches. Although these experimental results are specific, they indicate more general behavior trends; thus, the following observations may be made:

(1) For all projectile-shield material combinations, there is a shield angle below which ricochet occurs and above which perforation occurs. This angle is a function of projectile and shield material, projectile velocity, shield thickness, and impact angle. For Al → Al impacts when v = 25,000 fps, this angle is less than 10 degrees. For Ur → Mg impacts when v = 25,000 fps and t_s/d = 0.70, it is less than 2 degrees.

(2) At constant hypervelocity, the ratio of shield perforation area to projectile presented area (A_1/A_0) increases slowly from its value at $\alpha = 0^\circ$ (normal) to maximum in the region $\alpha < 60^\circ$, then decreases sharply as $\alpha \to 0^\circ$. The magnitude and angular location of this maximum is a function of the projectile and shield materials, projectile velocity, and shield thickness. For any projectile-shield combination, greater damage is sustained by the thicker shield (velocity constant).

(3) For normal impacts, the perforation area ratio (A_1/A_0) increases with approximately the first power of the impact velocity. However, for shield incident angles other than normal, although the perforation ratio (A_1/A_0) increases with velocity, the rate of increase decreases with increasing velocity.

(4) Increased velocity results in more complete fragmentation of both projectile and shield, and in a greater dispersal of these fragments. Fragment dispersal increases with an increase in shield thickness.

(5) Although spray angles are very difficult to define accurately, certain conclusions regarding their general behavior can be made. The projectile spray angle γ approaches zero degrees at some impact angle α^* where $\alpha^* > 0^\circ$ (velocity constant). This angle (α^*) may be predicted empirically using the shaped-charge primary penetration formula. The spall-spray angle θ also decreases with decreased angle of incidence (velocity constant). Its lower limit may be predicted when it is considered that perforation ceases to occur when $\theta = 0$.

(6) Total penetration of target structure has been shown to be a function of
   (a) projectile and target materials
   (b) projectile velocity
   (c) intersheet spacing
   (d) shield and target sheet angles of incidence

   Of all the variables considered, shield and target angle are the most critical, since rarely will a conical or cylindrical spacecraft be struck normally. It has been shown that damage to any target structure is primarily governed by the shield angle, α. To illustrate: with $v = 25,000$ fps and $s = 12$ inches, no target sheet perforation was noted with the shield normal to the projectile attack. When the shield angle was set at 25 degrees, however, the target sheet was perforated in all cases, regardless of orientation.

(7) The investigation of the phenomenon of impact flash may be summarized as follows:
   (a) Peak luminosity is independent of pressure in an inert atmosphere, and only above 1 torr is the surrounding air observed to have any significant effect.
   (b) With normal impact, peak luminosity is a direct function of the projectile presented area.
   (c) Peak luminosity (within the scope of the experiment) is independent of target sheet thickness. It should be noted that no tests have been performed using extremely thin foils as targets.
   (d) Peak luminosity has a power relationship with velocity. For Al → Al impacts, $I_p \propto v.^4$
   (e) Peak luminosity does not change significantly with changes of projectile impact angle.
   (f) Peak luminosity is independent of viewing angle.

REFERENCES

1. F.L. Whipple, "The Meteoric Risk to Space Vehicles," Vistas in Astronautics, Vol. 2, Pergamon Press, New York, 1958, pp. 115–124

2. D.R. Christman, J.W. Gehring, C.J. Maiden, and A.B. Wenzel, "Study of the Phenomena of Hypervelocity Impact," Summary Report, Contract NAS8-5067, GM DRL Report No. TR63-216, Santa Barbara, Calif., Jun 1963

3. "Aerospace Research Capabilities," GM DRL Report No. TR63-223 (Revised), Santa Barbara, Calif., Apr 1964

4. "Propulsion System Damage Study (U)," ASD-TDR-63-2, Vols. I, II and III, Eglin AFB, Florida, Jan 1964

5. S.M. Halperson, "Some Phenomena Associated with Impacts Into Aluminum," Proc. of the Sixth Symposium on Hypervelocity Impact, Vol. II, Part 2, Cleveland, Ohio, May 1963

6. J.W. Gehring and R.L. Warnica, "Summary Report on Hypervelocity Impact Experiments," Contract AF 08(635)-2783, ASD-TDR-64-5, Eglin AFB, Florida, Feb 1964

7. D.R. Nysmith and J.L. Summers, "An Experimental Investigation of the Impact Resistance of Double-Sheet Structures at Velocities to 24,000 Feet/Second," NASA TN-D-1431, Oct 1962

8. W. Herrmann and A.H. Jones, "Survey of Hypervelocity Impact Information," Massachusetts Institute of Technology, Aeroelastic and Structures Research Laboratory, ASRL Report No. 83-1, Sep 1961

9. C.J. Maiden, J.W. Gehring, and A.R. McMillan, "Investigation of Fundamental Mechanism of Damage to Thin Targets by Hypervelocity Projectiles," Semiannual Report, Contract ARPA Nonr-3891(00)(X), General Motors Corporation, GM Defense Research Laboratories, Report No. TR63-208, Mar 1963. See also, C.J. Maiden, "Experimental and Theoretical Results Concerning the Protective Ability of a Thin Shield Against Hypervelocity Projectiles," Proc. of Sixth Hypervelocity Impact Symposium, Vol. III, Cleveland, Ohio, May 1963

10. C.J. Maiden, J.W. Gehring, and A.R. McMillan, "Investigation of Fundamental Mechanism of Damage to Thin Targets by Hypervelocity Projectiles," General Motors Corporation, GM Defense Research Laboratories Final Report, Contract ARPA Nonr-3891(00)(X), GM DRL Report No. TR63-225, Santa Barbara, Calif., Sep 1963

11. R.L. Bjork, "Meteoroids vs. Space Vehicles," ARS J., Vol. 31, No. 6, Jun 1961, pp. 803-807

12. A.C. Charters and J.L. Summers, "High-Speed Impact of Metal Projectiles in Targets of Various Materials," Proc. of the Third Symposium on Hypervelocity Impact, Armour Research Foundation, Chicago, Feb 1959

13. R.J. Eichelberger and J.W. Gehring, "Effects of Meteoroid Impact on Space Vehicles," ARS J., Vol. 32, No. 10, Oct 1962, pp. 1583-1591

14. W. Herrmann and A.H. Jones, "Correlation of Hypervelocity Impact Data," Proc. of the Fifth Symposium on Hypervelocity Impact, Colorado School of Mines, Nonr-(G)-0020-62(X), Vol. 1 Part 2, Apr 1962

15. E.P. Bruce, "An Experimental Evaluation of Hypervelocity Impact Effects on Spacecraft Structures (U)," GE MSD-RSD, GE Document No. 63SD819, Sep 1963

16. R.W. Watson, K.R. Becker, and F.C. Gibson, "Thin Plate Perforation Studies in the Velocity Range from 2 to 5 km/sec," Proc. of the Sixth Hypervelocity Impact Symposium, Vol. III, Cleveland, Ohio, May 1963

17. J.W. Gehring and D.W. Sieck, "Reaction of the Lunar Surface to the Impact of a Lunar Probe," Progress in Astronautics and Aeronautics," Vol. 10, Technology of Lunar Exploration, Academic Press, New York, 1963, pp. 97-136 (for a more complete discussion, see J.W. Gehring and R.L. Warnica, "An Investigation of the Phenomena of Impact Flash and Its Potential Use as a Hit Detection and Target Discrimination Technique," Proc. of Sixth Hypervelocity Impact Symposium, Vol. II, Part 2, Cleveland, Ohio, May 1963; J.W. Gehring, A.C. Charters, and R.L. Warnica, "Meteoroid Impact on the Lunar Surface," (paper presented at the Lunar Surface Material Conference, Boston, Massachusetts, May 21-23, 1963))

APPENDIX I

DATA
HYPERVELOCITY IMPACT DAMAGE

The following tables present the raw data gathered under the experimental portion of the program. The units are as follows:

(1) All length measurements: inches
(2) Velocity: feet-per-second
(3) Weight: grams
(4) Area: square inches

The errors on the data are as follows:

(1) Projectile weight: ± .005 gram
(2) Projectile diameter: ± .0005 inch
(3) Projectile velocity: ± 1%
(4) Sheet thickness: ± .001 inch
(5) Sheet spacing: ± .125 inch
(6) All hole and crater diamensions: ± .001 inch

The measurements D_p and D_s (in inches) are defined in the text.

(This page is intentionally blank)

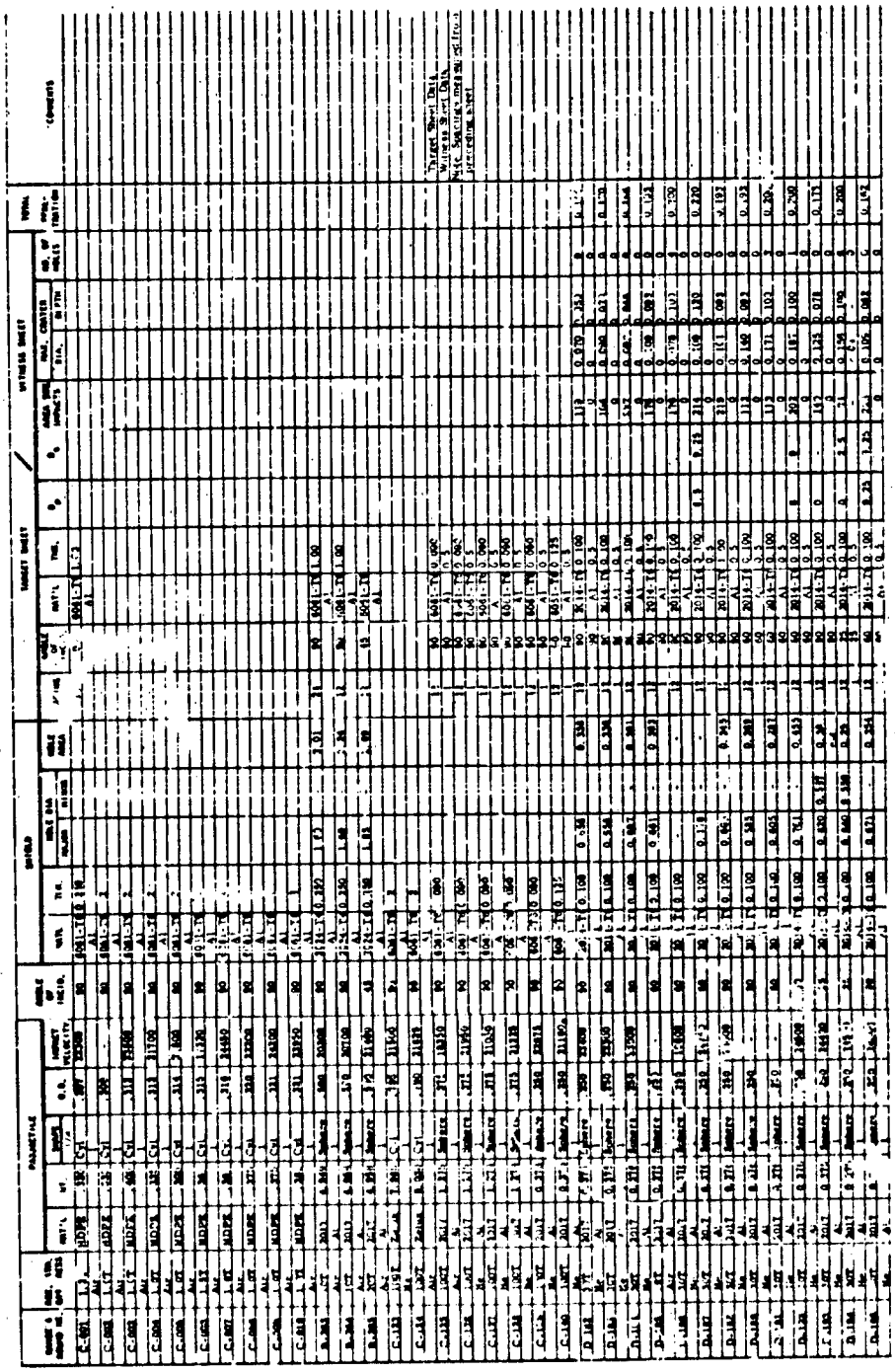

RANGE & ROUND NO.	AMB. ATM GAS. PRESS	PROJECTILE					ANGLE OF INCID.	SHIELD					TARGET SHEET						WITNESS SHEET				TOTAL	COMMENTS
		MAT'L	WT.	SHAPE l/d	D.D.	IMPACT VELOCITY		MAT'L	THK.	HOLE DIA MAJOR	HOLE DIA MINOR	HOLE AREA	SPACING	ANGLE OF INCID.	MAT'L	THK.	P_p	P_s	AREA SUR. IMPACTS	MAX. CRATER DIA.	MAX. CRATER DEPTH	NO. OF HOLES	PENETRATION	
D-186	30T	2017	0.374	Sphere	.350	25100	25	2014-T6	0.100	0.940	0.656	0.43	12	60	2014-T6	0.100	1.25	5	300	0.156	0.100	5	0.200	
	He	Al		1				Al				est.	1	6	Al	0.5			0	0	0	2		
D-187	30T	2017	0.374	Sphere	.350	24750	60	2014-T6	0.100	0.687	-	0.370	12	25	2014-T6	0.120	5.75	4	95	0.093	0.094	0	0.194	
	He	Al		1				Al					1		Al	0.5			0	0	0	0		
D-188	30T	2017	0.375	Sphere	.350	-	90	2014-T6	0.100	0.562		0.248	12		2014-T6	0.130			58	0.125	0.093	0	0.182	
	He	Al		1				Al					1		Al	0.5			0	0	0	0		
D-202	30T	2017	0.375	Sphere	.350	24500	60	2014-T6	0.100	-	-	-	12		2014-T6	0.100	9.5	9.5	-	-	-	-	-	
	He	Al		1				Al					1	6	Al	0.5			-	-	-	-		
C-368	10T	2017	0.375	Sphere	.350	25000	60	2014-T6	0.100	0.687	-	0.370	24	60	2014-T6	0.100	9	9	177	0.062	0.031	0	0.131	
	Air	Al		1				Al					1		Al	0.5			0	0	0	0		
C-369	10T	2017	1.372	Sphere	.375	4600	90	2014-T6	0.130	0.875	-	0.60	12	90	2014-T6	0.100			201	0.062	0.062	0	0.162	
	Air	Al		1				Al					1	90	Al	0.5			0	0	0	0		
C-370	10T	2017	1.372	Sphere	.375	24000	90	2014-T6	0.130	0.880	-	0.623	12	90	2014-T6	0.100	8	8	201	0.062	0.032	0	0.162	
	Air	Al		1				Al					1	90	Al	0.5			0	0	0	0		
C-384	1.0T	Zelux	1.084	Cyl	.620	31350																		No target
	Air			1																				
C-385	100T	2017	0.370	Sphere	.350	24100	90	2014-T6	0.100	0.687	-	0.370	24	90	2014-T6	0.100	19	19	660	0.047	0.031	0	0.131	
	He	Al		1				Al					1	90	Al	0.5			0	0	0	0		
C-386	100T	2017	0.370	Sphere	.350	23700	60	2014-T6	0.100	0.687	-	0.370	24	90	2014-T6	0.100			415	0.125	0.080	0	0.180	
	He	Al		1				Al					1	90	Al	0.5			0	0	0	0		
C-387	100T	2017	0.375	Sphere	.350	23100	25	2014-T6	0.100	0.800	0.540	0.310	24	90	2014-T6	0.100	-		-	-		-	-	
	He	Al		1		est.		Al					1	60	20 Al	0.5			-	-		-		
C-388	50T	2017	0.375	Sphere	.350	25100	90	2014-T6	0.100	0.687	-	0.370	24	60	2014-T6	0.100	21	21	755	0.047	0.031	0	0.131	
	He	Al		1				Al					1	60	Al	0.5			0	0	0	0		
C-389	25T	2017	0.375	Sphere	.350	25100	60	2014-T6	0.100	0.718	-	0.404	24	60	2014-T6	0.100	12	16.5	432	0.094	0.065	?	0.185	
	He	Al		1				Al					1	60	Al	0.5			0	0	0	0		
C-390	50T	2017	0.375	Sphere	.350	-	25	2014-T6	0.100	0.820	1.600	0.368	24	60	2014-T6	0.100			227	0.156	0.085	0	0.185	
	He	Al		1				Al					1	60	Al	0.5			0	0	0	5		
C-391	50T	2017	0.373	Sphere	.350	25600	25	2014-T6	.100	.840	.505	.34	24	60	2014-T6	.100	0	9	452	.172	.100	3	.200	
	He	Al		1				Al					1	60	Al	.5			0	0	0	0		
C-392	50T	2017	0.375	Sphere	.350	25500	90	2014-T6	.100	.718	-	.404	24	25	2014-T6	.100	17	17	284	.047	.031	0	.131	
	He	Al		1				Al					1	25	Al	.5			0	0		0		
C-393	50T	2017	0.375	Sphere	.350	25600	60	2014-T6	.100	.750	-	.442	24	25	2014-T6	.100	10.5	8	227	.062	.031	0	.131	
	He	Al		1				Al					1	25	Al				0	0	0	0		
C-394	50T	2017	0.375	Sphere	.350	24800	25	2014-T6	.100	.840	.500	.37	24	25	2014-T6	.100	0	5.5	95	.125	.100	6	.215	
	He	Al		1				Al					1	25	Al	.5			0.8	.032	0.5	0		
C-395	50T	2017	0.375	Sphere	.350	24750	60	2014-T6	.100	.718	-	.404	24	90	2014-T6	.100	12	18	491	.093	.100	0	.180	
	He	Al		1		est.		Al					1	90	Al	.5			0	0	0	0		
C-396	50T	2017	0.375	Sphere	.350	25500	25	2014-T6	.100	.840	[illegible]	.368	24	90	2014-T6	.100	0		1000	.218	.100	0	.200	
	He	Al		1		est.		Al					1	90	Al	.5			0	0	0	0		
C-397	50T	2017	1.373	Sphere	.375	[illegible]	60	2014-T6	.100	.875	-	.601	24	90	2014-T6	.100			707	.125	.100	21	.200	
	He	Al		1				Al					1	90	Al	.5			-	0	0	0		
C-398	50T	2017	1.37	Sphere	.375	24400	60	2014-T6	.100	.875	-	.601	24	60	2014-T6	.100	12	17	707	.100	.100	21	.200	
	He	Al		1				Al					1	62	Al	.5			-	0	0	0		
C-399	50T	2017	1.37	Sphere	.375	24200	60	2014-T6	.100	.860	-	.580	12	60	2014-T6	.100	6.5	9	337	.125	.100	-	[illegible]	
	He	Al		1				Al					1	60	Al	.5			3.4	0	0	0		
C-400	50T	2017	1.37	Sphere	.375	24325	25	2014-T6	.100	1.200	.380	[illegible]	12	61	2014-T6	.100	1.25	4.25	201	.187	.100	-	.282	
	He	Al		1				Al		est.			-	61	Al	.5			64	.062	.062	0		
C-401	50T	2017	1.37	Sphere	.375	-	90	2014-T6	.100	.850	-	.570	24	92	2014-T6	.100			755	.078	.047	0	.147	
	He	Al		1				Al					1	92	Al	-			0	0	0	0		
C-402	50T	2017	1.27	Sphere	.375	25000	90	2014-T6	.100	.850	-	.570	24	90	2014-T6	.100	19.75	19.75	755	.062	.047	0	.147	
	He	Al		1				Al					1	90	Al	.5			0	0	0	0		
C-403	50T	2017	1.27	Sphere	.375	25000	90	2014-T6	.175	.875	-	.601	24	60	2014-T6	.100	19	19	755	.062	.047	0	.147	
	He	Al		1				Al					1	60	Al	.5			0	0	0	0		
[illegible]	50T	2017	1.27	Sphere	.375	-	90	2014-T6	.100	.921	-	.665	12	60	2014-T6	.100			314	.062	.078	0	.178	
	He	Al		1				Al					-	60	Al	.5			0	0	0	0		
[illegible]	50T	2017	1.27	Sphere	.375	23820	90	2014-T6	.100	.843	-	.558	12	60	2014-T6	.100			201	.109	.093	0	.183	
	He	Al		1				Al					1	60	Al	.5			0	0	0	0		

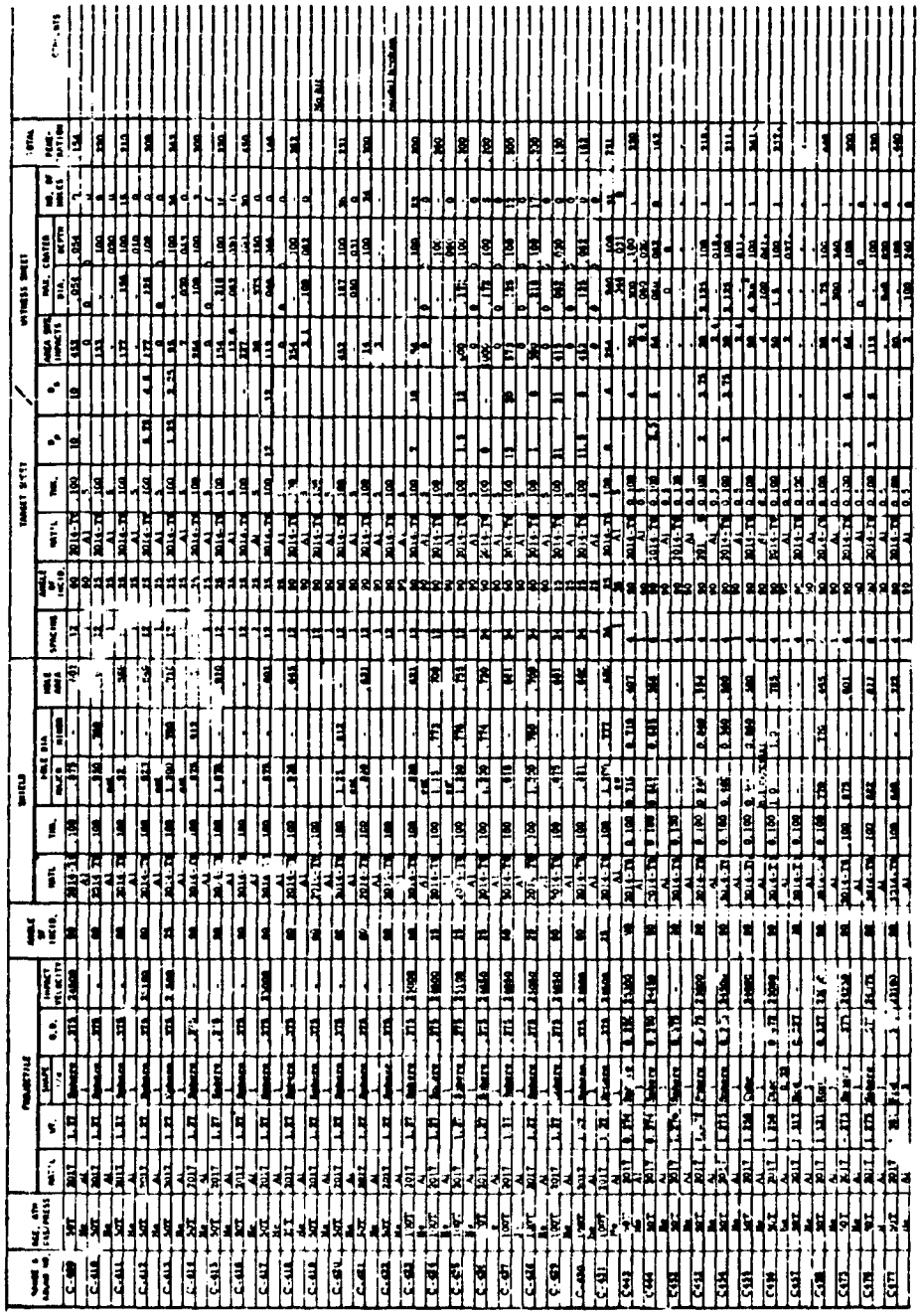

RANGE & ROUND NO.	ATM. GAS/PRESS	PROJECTILE MAT'L	PROJECTILE WT.	PROJECTILE SHAPE	PROJECTILE O.D.	PROJECTILE IMPACT VELOCITY	ANGLE OF INCID.	SHIELD MATL	SHIELD THK.	SHIELD HOLE DIA MAJOR	SHIELD HOLE DIA MINOR	SHIELD HOLE AREA	SPACING	ANGLE OF INCID.	TARGET SHEET MAT'L	TARGET SHEET THK.	θ_p	θ_s	WITNESS SHEET AREA SUBJ IMPACTS	WITNESS SHEET MAX. CRATER DIA.	WITNESS SHEET MAX. CRATER DEPTH	NO. OF HOLES	TOTAL PENETRATION	COMMENTS
C478	50T	2017	1.3[illegible]	Sphere	.375	[illegible]	45	2014-T6	.100	1.055	.877	.725	12	90	2014-T6	0.100	8	11.75	284	-	.100	-	.240	
	He	Al		1				Al					1	90	Al	0.5			7	.080	.040			
C479	50T	2017	1.374	Sphere	.375	24400	30	2014-T6	.100	1.18	.914	.717	9	30	2014-T6	0.100	2	8	200	-	.100		.201	
	He	Al		1				Al					1	[illegible]	Al	0.5			9.6	.320	.180	C		
C480	50T	2017	1.373	Sphere	.375	25100	10	2014-T6	.1[illegible]	1.24	[illegible]	[illegible]	7.[illegible]	10	2014-T6	0.100	0	-	-	-	-	-	-	
	He	Al		1				Al					1	[illegible]	Al	0.5								
C481	50T	2017	0.375	Sphere	.25	-	10	2014-T6	.100	-	-		12	80	2014-T6	0.100		-	-	-	-	-	-	no hit
	He	Al		1				Al					1	80	Al	0.5								
C482	50T	2017	0.375	Sphere	.250	-	45	2014-T6	.100	-	-	-	12	20	2014-T6	0.100		-	-	-	-	-		no hit
	He	Al		1				Al					1	20	Al	0.5								
[illegible]	50T	2017	0.047	Sphere	0.125	-	30	2014-T6	0.050	0.276	0.131	0.031												
	He	Al		1				Al																
[illegible]	50T	2017	0.047	Sphere	0.125	8325	20	2014-T6	0.050	0.257	0.140	0.0[illegible]5												
	He	Al		1				Al																
C561	50T	2017	0.047	Sphere	0.125	8306	30	2014-T6	0.050	0.275	0.178	0.038												
	He	Al		1				Al																
C562	50T	2017	0.047	Sphere	0.125	8028	40	2014-T6	0.050	0.284	0.197	0.044												
	He	Al		1				Al																
C563	10T	2017	0.047	Sphere	0.125	8165	50	2014-T6	0.050	0.384	0.220	0.241												
	He	Al		1				Al																
C564	10T	2017	0.047	Sphere	0.125	8015	60	2014-T6	0.050	0.3[illegible]	0.200	0.634												
	He	Al		1				Al																
C565	10T	2017	0.047	Sphere	0.125	8180	70	2014-T6	0.050	0.215	0.207	0.337												
	He	Al		1				Al																
C566	10T	2017	0.047	Sphere	0.125	8258	80	2014-T6	0.050	0.303	0.303	0.0724												
	He	Al		1				Al																
C567	10T	2017	0.047	Sphere	0.125	8200	90	2014-T6	0.050	0.200	0.200	0.0314												
	He	Al		1				Al																
[illegible]	50T	2017	0.370	Sphere	0.250	14900	90	2014-T6	0.100	.132	.532	0.322	12	90	2014-T6	0.100			112	0.130	0.080	0	0.180	
	Air	Al		1		[illegible]		Al					1	95	Al	0.5			0	0	0	0		
D097	50T	2017	0.370	Sphere	0.250	20400	90	2014-T6	0.100	.640	.640	0.322	12	90	2014-T6	0.100	5.5	7.5	200	0.080	0.050	0	0.150	
	Air	Al		1				Al					1	95	Al	0.5			0	0	0	0		
D098	50T	2017	0.375	Sphere	0.250	15300	60	2014-T6	0.100	.813	.516	0.365	12	60	2014-T6	0.100	3	4	132	0.160	0.100	4	0.200	
	Air	Al		1		[illegible]		Al					1	60	Al	0.5			0	0	0	0		
D099	50T	2017	0.375	Sphere	0.250	20900	60	2014-T6	0.101	.812	.665	0.365	12	60	2014-T6	0.100	5	6.5	200	0.100	0.080	0	0.180	
	Air	Al		1				Al					1	60	Al	0.5			0	0	0	0		
D101	50T	2017	0.375	Sphere	0.250	20300	25	2014-T6	0.101	.800	.532	0.315	12	25	2014-T6	0.100	[illegible]		50	0.160	0.100	0	0.200	
	Air	Al		1				Al					1	25	Al	0.5			0	0	0	0		
[illegible]	50T	2017	0.375	Sphere	0.250	15030	25	2014-T6	0.100	.720	.480	0.280	12	25	2014-T6	0.100	0		33	0.106	0.100	4	[illegible]	
	Air	Al		1				Al					1	25	Al	0.5			0	0	0	0		
[illegible]	100T	Nickel	1.480	Sphere	0.188	24730	90	2014-T6	0.100	.530	.530	0.220	12	90	2014-T6	0.100	4.5			0.120	0.100	many	0.260	
	He	200		1				Al					1	90	Al	0.5				0.040	0.060			
[illegible]	100T	Nickel	1.50	Sphere	0.270	-	90	2014-T6	0.100	-	-	-	12	90	2014-T6	0.100	-	-	-	-	-	-	-	Sabot broke up
	He	200		1				Al					1	90	Al	0.5			-	-	-	-		
[illegible]	100T	Nickel	1.48	Sphere	0.270	-	90	2014-T6	0.100	-	-	-	12	90	2014-T6	0.100	-	-	-	-	-	-	-	Sabot broke up
	He	200		1				Al					1	90	Al	0.5			-	-	-	-	-	
[illegible]	50T	Nickel	1.36	Sphere	0.27[illegible]	-	90	2014-T6	0.100	-	-	-	12	90	2014-T6	0.100	-	-	-	-	-	-	-	Sabot broke up
	He	200		1				Al					1	90	Al	0.5			-	-	-	-	-	
C597	50T	2017	[illegible].373	Sphere	0.250	25400	45	2014-T6	0.100	.780	.800	0.446	12	90	2014-T6	0.100	4.5	11.5		0.140	0.100	6	0.220	
	He	Al		1				Al					1	90	Al	0.5				0.060	0.020	0		
[illegible]	100T	2017	2.373	Sphere	0.25[illegible]	25500	35	2014-T6	0.100	.780	.640	0.[illegible]08	12	90	2014-T6	0.100	3.5	10.5		0.140	0.100	1	0.220	
	He	Al		1				Al					1	90	Al	0.5				0	0	0		
[illegible]	25T	2017	0.375	Sphere	0.2[illegible]	-	35	2014-T6	0.100	-	-	-	12	90	2014-T6	0.1[illegible]	-	-	-	-	-	-	-	No hit
	He	Al		1				Al					1	90	Al	0.5			-	-	-	-		
C599	50T	2017	0.375	Sphere	0.250	25300	35	2014-T6	0.100	.800	.683	0.429	12	30	2014-T6	0.100	3	10.75		0.380	0.100	2	0.201	
	He	Al		1				Al					1	90	Al	0.5				0	0	0		
C602	50T	2017	0.273	Sphere	0.250	2550[illegible]	10	2014-T6	0.100	.580/.550	.520	0.130	13.25	90	2014-T6	0.100	0	-		0	0	C	0.100	X-ray record
	He	Al		1				Al					1	90	Al	0.5				0	0	0		
C603	50T	Nickel	0.407	Sphere	0.187	-	80	2014-T6	0.100	-	-	-	12	80	2014-T6	0.100	-	-	-	-	-	-	-	No hit
	He	200		1				Al					1	80	Al	0.5			-	-	-	-		

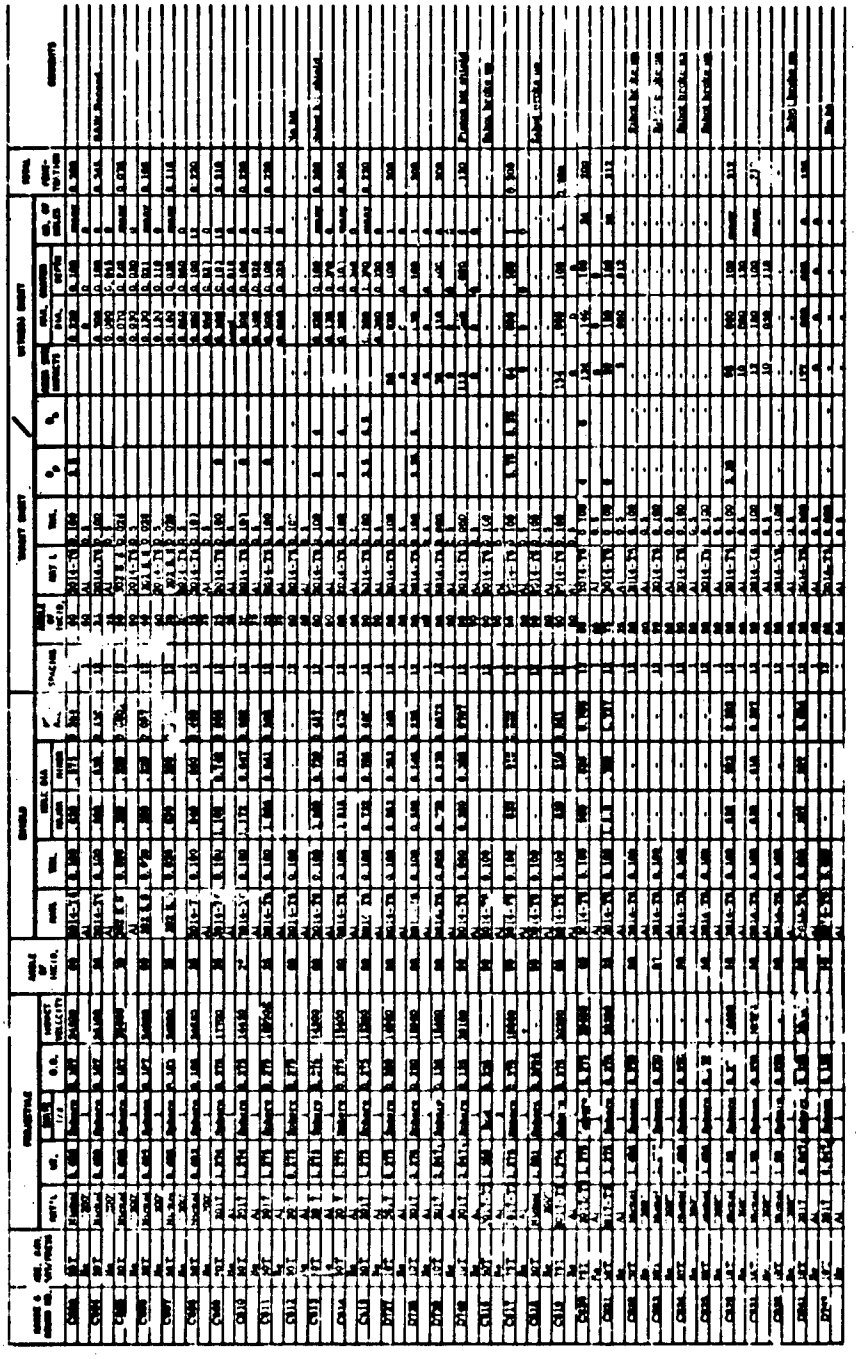

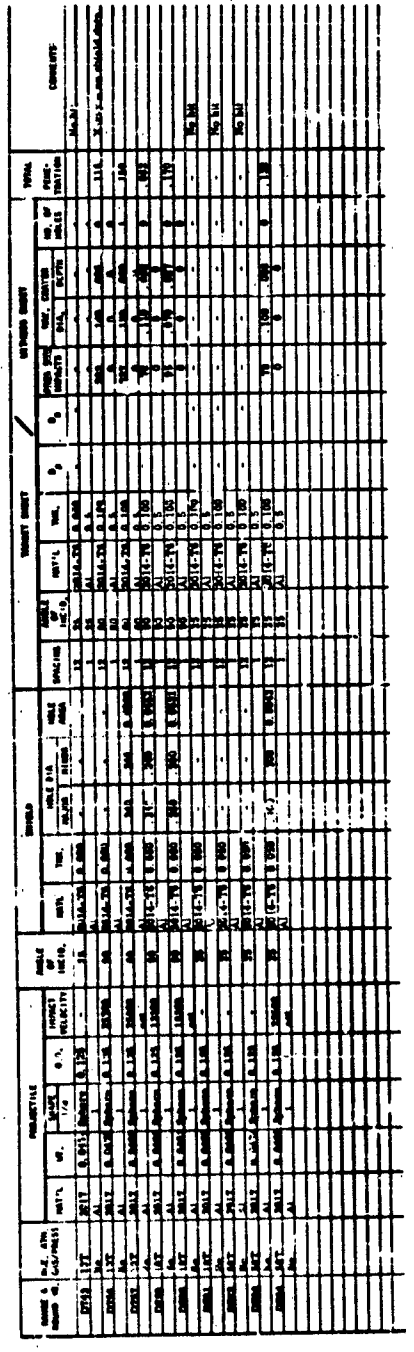

APPENDIX II

DATA
IMPACT FLASH PHENOMENON

The following tables present the raw data gathered under the experimental portion of the program. The units are as follows:

(1) Pressure: torr (mm of Hg)
(2) OD: inches
(3) Impact velocity: feet-per-second
(4) I_p: watts per steradian
(5) t_{peak}: microseconds

Instrumentation identification is as follows:

Channel	Instrument Range	Viewing Angle
1	1μ to 5.5μ	Normal to flight line
2	1μ to 5.5μ	Flight line (parallel)
3	0.594μ to 1μ	Normal to flight line
4	0.594μ to 1μ	Flight line (parallel)
4A	0.45μ to 1μ	Flight line (parallel)
5	0.18μ to 0.55μ	Flight line (parallel)

Numbers in parentheses (e.g., (10X)), refer to neutral density filter factors. An "S" after I_p results indicates that the channel was saturated and hence data is doubtful.

(This page is intentionally blank)

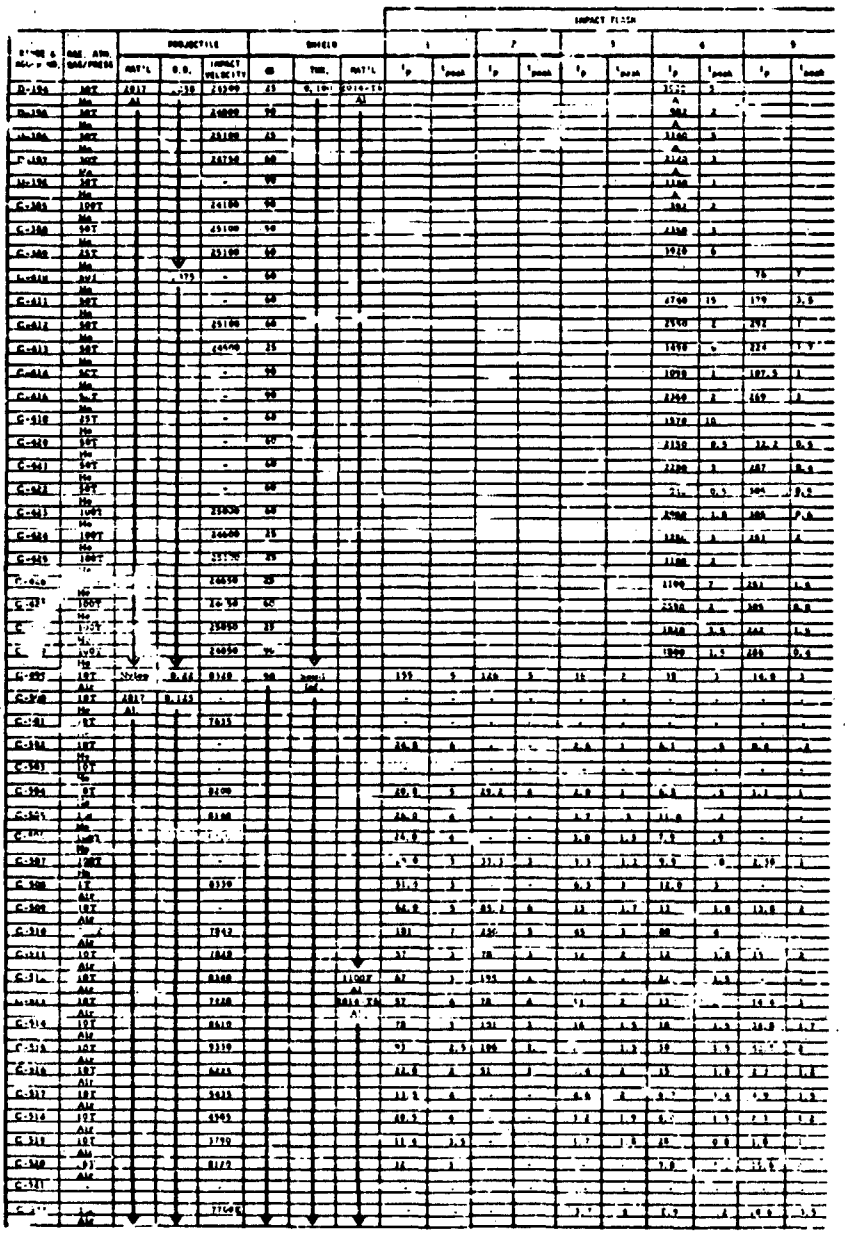

[redacted]

RANGE & ROUND NO.	AGE, ATM, GAS/PRESS	PROJECTILE			SHIELD			IMPACT FLA* 1		2		3		4		5	
		MAT'L	O.D.	IMPACT VELOCITY	θ	THK.	MAT'L	t_p	t_{peak}	t_p	t_{peak}	t_p	t_{peak}	t_p	t_{peak}	t_p	t_{peak}
C-523	1 μ Air	2017 Al.	0.125	7620	90°	Semi-Inf.	2014-T6 Al.	13.5	4	-	-	5.2	3	13.0	.1	16.8	2.5
C-524	.35T Air			[illegible]				57	4	-	-	[illegible]	-	11.0	.2	[illegible]	4.5
C-525	1 μ Air			8200				31	3	-	-	.5	3	5.7	2.7	15.1	4.5
C-526	200 μ Air			8235				31	4	46.5	3	4.8	4.7	11	[illegible]	16.8	2.5
C-527	30 μ Air			8150				41.5	3	46.5	3	5.6	3.6	15	.4	19.8	4
C-528	90 μ Air			8070				36	3	-	-	4.5	3.3	12	.1	10.0	3
C-529	.65T Air			8070				57	2.5	74	2.5	5.6	2.5	14	3	14.6	2.5
C-530	50T Air			8530				[illegible]	4	282	4	22	2	31	2	-	-
C-531	100T Air			7920				165	5	230	[illegible]	34	3	61	3	51.5	2
C-532	45 μ He			-				21	3	39	3	3.7	.1	4.7	.1	14.2	4
C-533	.7 μ He			8010				31	4.5	-	-	3.0	.1	5.5	.1	11.5	5
C-534	-			-				-	-	-	-	-	-	-	-	-	-
C-535	90 μ He			8100				15.5	2	-	-	1.3	3	3.7	.1	3.9	2.5
C-536	.7T He			8490				-	-	-	-	1.2	.1	2.4	.1	7.0	2
C-537	.5T He			8120				33	.1	54.5	5	43	3	6.0	.3	18.[illegible]	3
C-538	1T He			8170				21	4	36.0	3	2.8	2.5	3.9	2.5	12.1	2
C-539	65T He			8140				-	-	39.8	3	3.3	.1	3.1	.2	1.7	.5
C-540	200T He			7920				18.5	2.5	31.0	2	2.2	1.5	5.5	.7	1.7	[illegible]
C-541	10T Air			8300				62	2.5	84	2.5	13	1.5	18	1.3	28.7	1.6
C-542	10T Air			8610				66	2.3	101	2.5	17	1.4	16	.9	51	1
C-543	[illegible] Air			[illegible]				85	1.5	-	-	70	1.5	21	1	75	1.5
C-544	[illegible] He			[illegible]				16.5	3	39	4	1.4	.1	2.9	.1	6.7	[illegible]
C-545	[illegible]T He			7740				15.0	2	20	3	1.2	.1	2.6	[illegible]	-	-
C-546	6T He			8040				17.0	3	28	3	0.96	[illegible]	2.5	.2	-	-
C-547	20T He			8550				24	3	31	2.5	2.1	2	3.3	.6	1.7	1
C-548	30T He			8605				29	3.5	46.5	3.5	3.2	1.5	4.4	1	1.4	1
C-549	100T He			[illegible]				18.5	3	37	2.5	2.1	1.2	4.7	.9	0.92	.8
C-550	19 μ He			8400	80°			25	6	26	3	1.8	.1	3.1	.1	1.4	1.1
C-551				8190	70°			23	5	25	4	1.7	1.2	2.2	.2	1.1	1.2
C-552				8190	60°			37	3	33	3	1.9	2.5	2.2	2	0.9[illegible]	1
C-553				8300	50°			49	7	44	7	1.2	3	2.1	2	0.61	1
C-554				[illegible]	40°			56	8	46.5	8	0.60	4	1.4	4	0.29	1
C-555				8435	30°			67	10	4.8	17	1.8	8	2.1	.1	Too Small	-
C-556				8285	20°			27	18	21	27	-	-	-	-	"	-
C-557				8250	10°			25	10	15	30	-	-	-	-	"	-
C-558				8130	10°	0.050		-	-	-	-	-	-	-	-	-	-
C-559				-	10°			-	-	-	-	-	-	-	-	-	-
C-560				[illegible]	20°			23	19	-	-	-	-	-	-	-	-
C-561				[illegible]	30°			34	17	42	10	0.83	[illegible]	1.7	[illegible]	[illegible]	2
C-562				[illegible]	40°			-	-	20	7	1.2	3	[illegible]	[illegible]	0.17	1
C-563				8165	50°			29	5	[illegible]	5	2.1	[illegible]	1.9	[illegible]	0.44	[illegible]
C-564				[illegible]	60°			40	3	40	5	1.4	.2	1.6	.3	0.74	1.9
C-565				8180	70°			31	4	43	3	0.97	.4	[illegible]	.2	1.4	1.2
C-566				[illegible]	80°			25	3	11	3	1.0	.3	1.4	.2	.4	1
C-567				8206	90°			39	4	44	3	0.97	1	1.1	.3	1.9	1.1
C-568				7330				28	4	54	3	[illegible]	.2	4.9	.4	1.2	1.2
C-569				[illegible]				16.5	1.2	78	3	0.37	.4	1.2	.4	0.55	3
C-570				[illegible]				24	4	14	4	0.41	1	1.1	.1	0.16	.4

[redacted]

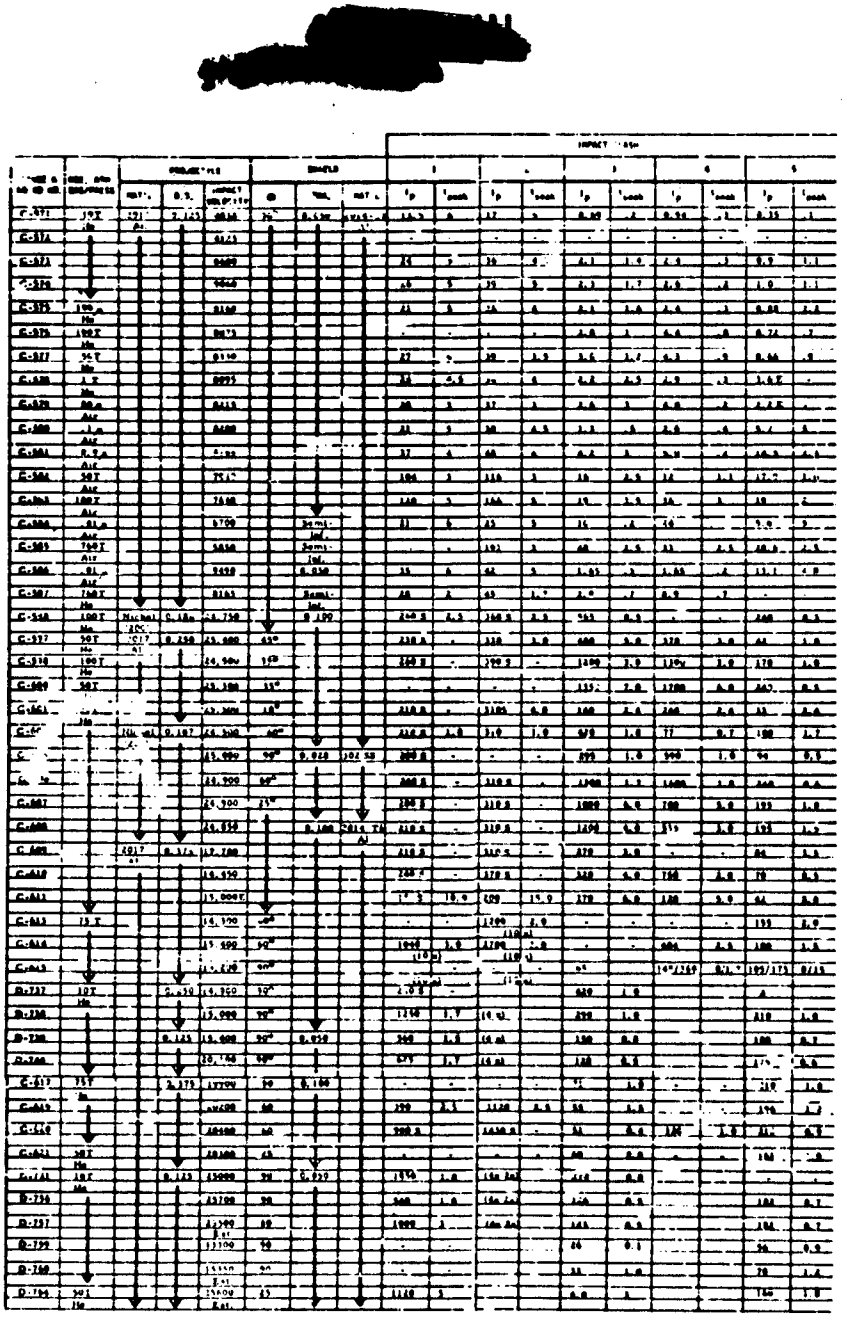

3	PICATINNY ARSENAL (SMUPA-DW8)
1	FRANKFORD ARSENAL (Lib)
1	SPRINGFIELD ARMORY (SWESP-RD/P.F.Foley)
1	US ARMY RESCH OFFICE-DURHAM (CRD-AA-IP
1	BALLISTIC RESCH LAB (AMXBR-X)
2	BALLISTIC RESCH LAB (Tech Lib)
3	BALLISTIC RESCH LAB (AMXBR-T)
1	BALLISTIC RESCH LAB (AMXBR-WC)
20	DDC
2	DIR USAF PROJ RAND
2	AEROJET GEN CORP (Mr. R. B. Mortensen)
2	GENERAL MOTORS CORP (Mr. J. W. Gehring)
3	THE BOEING CO. (Mr. J. F. Lundeberg/R. Elam)
2	GENERAL ELECTRIC CO. MSVD
2	ARO INC (VKF-AB/J. Payne)
1	AVCO CORP RAD (Mr. M. Rockowitz)
1	AEROSPACE CORP (Mr. V. Frost)
1	GENERAL ELECTRIC CO. (Dr. T. A. Riney)
1	AEROSPACE CORP (Mr. Tom Friedman)
1	SSD (SSZDS/Maj Sherline)
2	NAVAL ORDNANCE LABORATORY
1	NASA/LANGLEY RESCH CTR (Mr. E. Kurszewski)
1	PGF
4	PGBAP-1
1	ATBT
1	ATG
1	ATTR
4	ATWF

INITIAL DISTRIBUTION LIST

1 DOD P&T
3 ADVANCED RSCH PROJ AGENCY
(Mr. Koether)
1 WPNS SYS EVAL GP
2 DASA (Doc Lib Br)
1 HQ USAF (AFORQ-QT)
1 HQ USAF (AFRSTE)
1 HQ USAF (AFPSTB)
1 HQ USAF (AFCIN)
1 HQ USAF (AFRDP)
1 HQ USAF (AFOCE)
1 AFSC (SCTR)
1 AFSC (HSFA)
1 AFSC (SCSA)
1 ASD (ASJ)
1 AFAL (AVN)
1 AFML (MAA)
1 AFML (MAY)
2 AFFDL (FDTS)
1 FTD (TDFA)
1 FTD (TDCE)
1 FTD (TDPS)
1 FTD (TDBTA)
1 FTD (TELA)
1 FTD (NIDEWA)
1 SEG
1 SEG (SETGF)
1 SEG (SEDC)
1 SEC (SEBA)
1 SEC (SEPRR)
1 RTD (RTNW)
2 RTD (Tech Lib)
2 SSD (SSTAS/Capt Hartford)
1 SSD (SSTDS)
2 SSD (SSTFT)
2 BSD (BSVDA)
1 BSD (BSVDA/Capt Baker)
1 ESD (ESAT)
1 AFCRL (CFXL)
1 RADC (RAALD)
1 AEDC (AETV/Maj Brown)
2 AEDC (Tech Lib)
2 AFWL (WLL)
1 AFWL (WLRPT/Capt Gillespie)
1 AFWL (WLAX)
1 AFWL (WLRPD)
1 AFMTC (MTBAT)
1 AFFTC (FTOOT)
1 SAC (OA)

1 AU (AUL-8754)
1 NASA
1 NASA/LEWIS RESCH CTR
2 NASA/AMES RESCH CTR
1 NASA/LANGLEY RESCH CTR
1 NASA/MARSHALL SPACE FLIGHT CTR
1 US ATOMIC ENERGY COMM
1 DEPT OF THE INTERIOR
2 OFFICE OF NAVAL RESCH
1 US NAVAL ORD LAB (Lib)
1 US NAVAL WPNS EVAL FACILITY
1 US NAVAL WPNS LAB (Lib)
3 NAVAL RESCH LAB (Code 6240)
2 NAVAL RSCH LAB (Tech Lib)
1 US NAVAL ORD LAB
2 NAVAL ORDNANCE TEST STN
1 MARTIN-MARIETTA CORP
(Mr. W. R. Porter)
1 NORTRONICS DIV OF NORTHROP CORP
(Mr. B. Karin)
1 RAYTHEON CO.
(Msl Sys Div, W. Hurd)
1 GENERAL ELECTRIC CO.
(Mr. G. Ashley)
2 RSCH INST - ILLINOIS INST OF TECH
2 BATTELLE MEMORIAL INSTITUTE
3 AEROSPACE CORP
(Mr. D. Singer)
1 SHOCK HYDRODYNAMICS INC
(Mr. R. J. Bjork)
1 GENERAL DYNAMICS CORP
(Mr. M. Walsh)
1 PHYSICS INTERNATIONAL
(Mr. J. Harlan)
2 GENERAL DYNAMICS CORP
2 SCIENTIFIC & TECH INFO FAC
(NASA Rep (SAK/DL)
2 LOCKHEED AIRCRAFT CORP
2 AEROSPACE CORP (Tech Lib)
2 AEROSPACE CORP
2 AEROSPACE CORP
1 AEROSPACE CORP
2 US ARMY
2 USA MSL COMD (Tech Lib)
1 ARMY MATERIEL COMMAND
(AMCRD-DE-W)
1 ARMY WEAPONS COMMAND
(AMSWE-RDW)
1 FIELD COMMAND DASA (FCDR)
2 PICATINNY ARSENAL (Tech Lib)

UNCLASSIFIED

Security Classification

14 KEY WORDS	LINK A		LINK B		LINK C	
	ROLE	WT	ROLE	WT	ROLE	WT
Hypervelocity projectiles						
Impact flash						
Impact shock						
Hypervelocity guns						
Fragmentation						
Kill probabilities						

INSTRUCTIONS

1. ORIGINATING ACTIVITY: Enter the name and address of the contractor, subcontractor, grantee, Department of Defense activity or other organization *(corporate author)* issuing the report.

2a. REPORT SECURITY CLASSIFICATION: Enter the overall security classification of the report. Indicate whether "Restricted Data" is included. Marking is to be in accordance with appropriate security regulations.

2b. GROUP: Automatic downgrading is specified in DoD Directive 5200.10 and Armed Forces Industrial Manual. Enter the group number. Also, when applicable show that optional markings have been used for Group 3 or Group 4 as authorized.

3. REPORT TITLE: Enter the complete report title in all capital letters. Titles in all cases should be unclassified. If a meaningful title cannot be selected without classification, show title classification in all capitals in parenthesis immediately following the title.

4. DESCRIPTIVE NOTES: If appropriate, enter the type of report, e.g., interim, progress, summary, annual, or final. Give the inclusive dates when a specific reporting period is covered.

5. AUTHOR(S): Enter the name(s) of author(s) as shown on or in the report. Enter last name, first name, middle initial. If military, show rank and branch of service. The name of the principal author is an absolute minimum requirement.

6. REPORT DATE: Enter the date of the report as day, month, year, or month, year. If more than one date appears on the report, use date of publication.

7a. TOTAL NUMBER OF PAGES: The total page count should follow normal pagination procedures, i.e., enter the number of pages containing information.

7b. NUMBER OF REFERENCES: Enter the total number of references cited in the report.

8a. CONTRACT OR GRANT NUMBER: If appropriate, enter the applicable number of the contract or grant under which the report was written.

8b, 8c, & 8d. PROJECT NUMBER: Enter the appropriate military department identification, such as project number, subproject number, system numbers, task number, etc.

9a. ORIGINATOR'S REPORT NUMBER(S): Enter the official report number by which the document will be identified and controlled by the originating activity. This number must be unique to this report.

9b. OTHER REPORT NUMBER(S): If the report has been assigned any other report numbers *(either by the originator or by the sponsor)*, also enter this number(s).

10. AVAILABILITY/LIMITATION NOTICES: Enter any limitations on further dissemination of the report, other than those imposed by security classification, using standard statements such as:

(1) "Qualified requesters may obtain copies of this report from DDC."

(2) "Foreign announcement and dissemination of this report by DDC is not authorized."

(3) "U. S. Government agencies may obtain copies of this report directly from DDC. Other qualified DDC users shall request through

_____."

(4) "U. S. military agencies may obtain copies of this report directly from DDC. Other qualified users shall request through

_____."

(5) "All distribution of this report is controlled. Qualified DDC users shall request through

_____."

If the report has been furnished to the Office of Technical Services, Department of Commerce, for sale to the public, indicate this fact and enter the price, if known.

11. SUPPLEMENTARY NOTES: Use for additional explanatory notes.

12. SPONSORING MILITARY ACTIVITY: Enter the name of the departmental project office or laboratory sponsoring *(paying for)* the research and development. Include address.

13. ABSTRACT. Enter an abstract giving a brief and factual summary of the document indicative of the report, even though it may also appear elsewhere in the body of the technical report. If additional space is required, a continuation sheet shall be attached.

It is highly desirable that the abstract of classified reports be unclassified. Each paragraph of the abstract shall end with an indication of the military security classification of the information in the paragraph, represented as (TS), (S), (C), or (U).

There is no limitation on the length of the abstract. However, the suggested length is from 150 to 225 words.

14. KEY WORDS: Key words are technically meaningful terms or short phrases that characterize a report and may be used as index entries for cataloging the report. Key words must be selected so that no security classification is required. Identifiers, such as equipment model designation, trade name, military project code name, geographic location, may be used as key words but will be followed by an indication of technical context. The assignment of links, rules, and weights is optional.

UNCLASSIFIED

Security Classification

UNCLASSIFIED

Security Classification

DOCUMENT CONTROL DATA - R&D

(Security classification of title, body of abstract and indexing annotation must be entered when the overall report is classified)

1. ORIGINATING ACTIVITY (Corporate author) General Motors Corporation, GM Defense Research Laboratories, Santa Barbara, California	2a. REPORT SECURITY CLASSIFICATION CONFIDENTIAL 2b. GROUP Gp-4

3. REPORT TITLE

HYPERVELOCITY IMPACT EXPERIMENTS

4. DESCRIPTIVE NOTES (Type of report and inclusive dates)

Final Technical Report - July 1964

5. AUTHOR(S) (Last name, first name, initial)

Warnica, R. L.
Gehring, J. W.

6. REPORT DATE	7a. TOTAL NO. OF PAGES	7b. NO. OF REFS
December 1964	68	17

8a. CONTRACT OR GRANT NO	9a. ORIGINATOR'S REPORT NUMBER(S)
AF 08(635)-2783	SBL-64-0417-S
b. PROJECT NO. 9850	
c.	9b. OTHER REPORT NO(S) (Any other numbers that may be assigned this report) ATI-TR-64-83
d.	

10. AVAILABILITY/LIMITATION NOTICES

Qualified requesters may obtain copies from DDC.

11. SUPPLEMENTARY NOTES	12. SPONSORING MILITARY ACTIVITY
	Det 4, Research and Technology Division Eglin Air Force Base, Florida

13. ABSTRACT

(U) This final report describes the experimental results of a program conducted under Contract AF 08(635)-2783, "Hypervelocity Impact Experiments," to investigate the vulnerability of multiple sheet thin target assemblies to hypervelocity projectiles impacting at both normal and oblique angles. This study of penetration, perforation and spalling was conducted using an accelerated-reservoir light-gas gun to launch projectiles to velocities ranging from 5000 fps to 25,500 fps. Projectile incident angles ranged from 90 degrees (normal) to 10 degrees. Target damage was evaluated in terms of hold area, depty of penetration and effected area. Damage was correlated with impact velocity, impact angle, projectile variables, and target variables.

DD FORM 1 JAN 64 1473

UNCLASSIFIED

Security Classification

UNCLASSIFIED

UNCLASSIFIED